

Instabilities and nonlinear dynamics of concentrated active suspensions

Barath Ezhilan,¹ Michael J. Shelley,² and David Saintillan^{1,a)}

¹*Department of Mechanical Science and Engineering, University of Illinois at Urbana-Champaign, Urbana, Illinois 61801, USA*

²*Courant Institute of Mathematical Sciences, New York University, New York, New York 10012, USA*

(Received 24 September 2012; accepted 6 June 2013; published online 18 July 2013)

Suspensions of active particles, such as motile microorganisms and artificial microswimmers, are known to undergo a transition to complex large-scale dynamics at high enough concentrations. While a number of models have demonstrated that hydrodynamic interactions can in some cases explain these dynamics, collective motion in experiments is typically observed at such high volume fractions that steric interactions between nearby swimmers are significant and cannot be neglected. This raises the question of the respective roles of steric vs hydrodynamic interactions in these dense systems, which we address in this paper using a continuum theory and numerical simulations. The model we propose is based on our previous kinetic theory for dilute suspensions, in which a conservation equation for the distribution function of particle configurations is coupled to the Stokes equations for the fluid motion [D. Saintillan and M. J. Shelley, “Instabilities, pattern formation, and mixing in active suspensions,” *Phys. Fluids* **20**, 123304 (2008)]. At high volume fractions, steric interactions are captured by extending classic models for concentrated suspensions of rodlike polymers, in which contacts between nearby particles cause them to align locally. In the absence of hydrodynamic interactions, this local alignment results in a transition from an isotropic base state to a nematic base state when volume fraction is increased. Using a linear stability analysis, we first investigate the hydrodynamic stability of both states. Our analysis shows that suspensions of pushers, or rear-actuated swimmers, typically become unstable in the isotropic state before the transition occurs; suspensions of pullers, or head-actuated swimmers, can also become unstable, though the emergence of unsteady flows in this case occurs at a higher concentration, above the nematic transition. These results are also confirmed using fully nonlinear numerical simulations in a periodic cubic domain, where pusher and puller suspensions are indeed both found to exhibit instabilities at sufficiently high volume fractions; these instabilities lead to unsteady chaotic states characterized by large-scale correlated motions and strong density fluctuations. While the dynamics in suspensions of pushers are similar to those previously reported in the dilute regime, the instability of pullers is novel and typically characterized by slower dynamics and weaker hydrodynamic velocities and active input power than in pusher suspensions at the same volume fraction. © 2013 AIP Publishing LLC. [<http://dx.doi.org/10.1063/1.4812822>]

I. INTRODUCTION

Suspensions of motile microorganisms can show fascinating and complex large-scale dynamics that have been aptly termed *bacterial turbulence*. The dynamics of such active suspensions are

^{a)}Electronic mail: dstn@illinois.edu.

characterized by persistent unsteadiness,¹ the creation and destruction of coherent flow structures,² enhanced fluid mixing,^{3,4} temporal and spatial fluctuations in swimmer concentration,² and dynamical transitions in the character of the system as system size³ and swimmer concentration⁵⁻⁷ are varied; see Ishikawa,⁸ Ramaswamy,⁹ Koch and Subramanian,¹⁰ and Saintillan and Shelley¹¹ for recent reviews of some of these phenomena.

Theoretical investigations have used a variety of approaches to predict, understand, and interpret these experiments. The active nematic theory of Simha and Ramaswamy¹² was an important early contribution. They posed a phenomenological continuum theory for the collective behavior of swimmers based upon previous classic models for nematic liquid crystals that included a destabilizing “active stress” generated by particle locomotion. This theory predicted, among other things, that in the Stokesian regime of negligible fluid inertia suspensions of swimmers with long-range orientational order would be unstable to hydrodynamic flows. There have since been other related theories. Examples include Aranson *et al.*,¹³ who developed a kinetic theory for the dynamics of a motile suspension in a thin fluid film where active fluid stresses as well as the alignment effects of pairwise swimmer collisions are modeled. Wolgemuth¹⁴ developed a two-phase (fluid and swimmer) model of a bacterial suspension driven by active stresses that incorporates nematic elasticity.

Another approach has been to model and directly simulate the hydrodynamic interactions of many swimmers, as well as trying to capture within these simulations the effect of steric interactions.¹⁵⁻²⁰ These simulations have reproduced qualitative aspects of experiments, such as the appearance of large-scale flows, and have shown that hydrodynamic interactions alone can be sufficient for producing collective dynamics and coherent structures. Recent work by Saintillan and Shelley¹⁸ that simulated large-scale suspensions of hydrodynamically interacting slender swimming rods demonstrated this latter point, as well as highlighted the importance of the swimming mechanism to the appearance of large-scale flows. These simulations showed that transitions can occur as a function of swimmer concentration and system size, and that unstable suspensions can exhibit local flocking and concentration fluctuations not predicted by linear theories.¹⁸

In seeking to understand experiments and their simulations of motile suspensions, Saintillan and Shelley^{21,22} developed a simple kinetic model based on first principles that couples a Smoluchowski equation for the distribution of particle configurations (positions and orientations) to the Stokes equations forced by the active stresses generated by the locomotion of the swimmers through the surrounding fluid (a similar model was also developed independently by Subramanian and Koch²³). This Smoluchowski/Stokes system of partial differential equations is very similar to that developed by Doi and Edwards²⁴ to describe passive Brownian rod suspensions, as the active stress tensor resulting from locomotion shares the same tensorial form as the Brownian stress resulting from thermal fluctuations in passive suspensions. (See Hatwalne *et al.*²⁵ for a discussion of the fundamental differences in origin and interpretation of active and passive nematogenic stresses, which are particularly relevant for ordered phases.) One very important difference is that the stresslet coefficient of the active stress is oppositely signed (negative) when the motile particles are *pushers* (rear-actuated swimmers). Both passive and active systems have an energy-like quantity, the relative conformational entropy, and for passive rods and (front-actuated) *pullers* this quantity decays to zero, implying global stability of the state of uniform isotropy. This is not so in the case of pushers, allowing the possibility of a continuous production of fluctuations from the swimmer motions and fluid coupling.

Two steady-state swimmer distributions play an important role for the kinetic theory of slender active particles. The first is the globally aligned “nematic” state, which requires neglect of rotational diffusion in the dilute limit when steric interactions are neglected. A linear analysis by Saintillan and Shelley²² showed its instability to hydrodynamic flow, in agreement with the earlier prediction of Simha and Ramaswamy.¹² The second state is uniform isotropy, and a linear analysis around it showed stability for suspensions of pullers, and an orientational instability for pushers if the system size or swimmer concentration is sufficiently high. For pullers, stability is global due to the monotonic decay of the system’s conformational relative entropy.²² These predictions, which are in qualitative agreement with experiments of bacterial suspensions within suspended films,²⁶ were also confirmed using continuum simulations,^{21,22,27} which for pushers showed the emergence, from near uniform isotropy, of large-scale roiling flows that are characterized by concentration fluctuations

and coherent structures. Puller suspensions showed relaxation to the uniform state. These dynamics are also consistent, at least qualitatively, with results from direct particle simulations.^{17,18}

It is widely accepted that at high concentrations, steric interactions between swimmers become important with the expectation that sterically induced nematic ordering will emerge. Certainly such ordering has been observed in the dynamics of dense bacterial suspensions,⁷ as well as in swarming flocks of motile bacteria,^{28–30} in which long-ranged fluid-mediated interactions may not always be significant. Simulations of self-propelled hard rods interacting solely via contact interactions in fact also show the emergence of coherent structures and correlated motions,³¹ raising the question of the relative roles of steric vs hydrodynamic interactions in dense active suspensions. In this paper, we attempt some understanding of the joint effects of both types of interactions by studying a simple and classical extension of our previous kinetic theory for dilute suspensions that accounts for local alignment as a result of steric interactions. In particular, we follow Doi and Edwards²⁴ in their modeling of steric interactions in dense rod suspensions, and use the local tensor order parameter of the particle orientation distribution to generate an alignment torque in the single particle fluxes. This torque is proportional to local rod concentration and stabilizes the locally aligned state against rotational diffusion. As this torque devolves from a force potential, it also generates a contribution to the extra stress which must be accounted for in the overall momentum balance.²⁴ Baskaran and Marchetti³² developed and studied the linear stability properties of a kinetic theory, after a moment closure approximation, rather similar to the one studied here. Forest *et al.*³³ also recently developed a related, yet more elaborate theory that includes liquid crystalline contributions, and which they have used to investigate pattern formation in two dimensions.

We first investigate the linear stability of the full extended kinetic model to plane-wave perturbations for both the isotropic and nematically ordered base states. We find that modes of instability are restricted generically to the zeroth, first, and second azimuthal modes on the sphere of orientations, and can be determined analytically in the long-wave limit for the isotropic base state. For pusher suspensions, we find that both isotropic and nematic states are expected to become unstable beyond a critical strength of steric coupling. For puller suspensions, hydrodynamic interactions are stabilizing in the dilute regime. However, increasing the strength of steric interactions destabilizes the isotropic base state, while the nematic state can likewise become unstable to hydrodynamic coupling. To investigate the fully nonlinear regimes, we then perform spectral/finite-difference simulations of the full kinetic equations in three dimensions. These simulations find some surprising behaviors, such as unexpected two-dimensional dynamics at low volume concentrations for pushers, and very different coherent structures in unstable pusher and puller suspensions. We investigate the degree of ordering that emerges in these simulations and generally find that the suspensions show large regions of nematic order that are nonetheless transitory and unsteady. This seems roughly consistent with experimental observations on flocks of motile bacteria.^{7,28–30} As in our previous dilute model, we find that the power input by swimming is considerably larger for pushers than for pullers, even in the unstable regimes, but find that, unlike our previous work, sterically mediated unstable puller suspensions can now also increase the power input to the system.

II. KINETIC MODEL

A. Conservation equation

We consider a suspension of N active particles of length ℓ and thickness b (aspect ratio $r = \ell/b \gg 1$) in a volume V assumed to be a cube of linear dimension $L = V^{1/3}$. The mean number density is defined as $n = N/V$, and we also introduce an effective volume fraction $\nu = nb\ell^2$, which is the appropriate parameter to capture the isotropic-to-nematic transition in the case of passive rodlike particles.²⁴ The model we use to study the dynamics is an extension of our previous kinetic theory for dilute suspensions of self-propelled particles^{21,22} to account for local alignment as a result of steric interactions. We describe the configuration of the suspension by means of a continuum distribution function $\Psi(\mathbf{x}, \mathbf{p}, t)$ of center of mass \mathbf{x} and director \mathbf{p} (where \mathbf{p} is a unit vector defining the orientation and swimming direction of the particles) at time t . By conservation of particles, $\Psi(\mathbf{x}, \mathbf{p}, t)$ satisfies

a Smoluchowski equation²⁴

$$\partial_t \Psi + \nabla_x \cdot (\dot{\mathbf{x}} \Psi) + \nabla_p \cdot (\dot{\mathbf{p}} \Psi) = 0, \quad (1)$$

where ∇_p denotes the gradient operator on the unit sphere of orientations Ω and is defined as

$$\nabla_p = (\mathbf{I} - \mathbf{p}\mathbf{p}) \cdot \frac{\partial}{\partial \mathbf{p}}, \quad (2)$$

and the distribution function is normalized as

$$\frac{1}{V} \int_V \int_\Omega \Psi(\mathbf{x}, \mathbf{p}, t) d\mathbf{p} d\mathbf{x} = n. \quad (3)$$

With this normalization, the constant distribution function $\Psi = n/4\pi$ corresponds to the uniform and isotropic state.

The flux velocities $\dot{\mathbf{x}}$ and $\dot{\mathbf{p}}$ in Eq. (1) describe the motion of the particles in the suspension and are modeled as

$$\dot{\mathbf{x}} = V_0 \mathbf{p} + \mathbf{u}(\mathbf{x}) - D \nabla_x \ln \Psi, \quad (4)$$

$$\dot{\mathbf{p}} = (\mathbf{I} - \mathbf{p}\mathbf{p}) \cdot \nabla_x \mathbf{u} \cdot \mathbf{p} - \nabla_p U(\mathbf{x}, \mathbf{p}) - d \nabla_p \ln \Psi. \quad (5)$$

In Eq. (4), the center-of-mass velocity is expressed as the sum of three contributions: the particle swimming velocity $V_0 \mathbf{p}$ (along the director \mathbf{p}), the local mean-field fluid velocity $\mathbf{u}(\mathbf{x})$, whose calculation is explained in Sec. II D, and translational diffusion with diffusivity D , assumed to be isotropic. Similarly, Eq. (5) models the angular flux velocity as the sum of three terms. The first term on the right-hand side uses Jeffery's equation^{34,35} to describe the rotation of a slender rodlike particle in the mean-field flow with velocity gradient $\nabla_x \mathbf{u}$. The second term, which will be discussed in Sec. II B, models steric interactions due to concentration effects by means of a local alignment torque deriving from a potential $U(\mathbf{x}, \mathbf{p}, t)$ that depends on the local particle orientations. Finally, Eq. (5) also captures rotational diffusion with angular diffusivity d .

From the distribution function, we also define the concentration field $c(\mathbf{x}, t)$, director field (or polar order parameter) $\mathbf{n}(\mathbf{x}, t)$, and nematic order parameter $\mathbf{Q}(\mathbf{x}, t)$, as the zeroth, first, and second moments of $\Psi(\mathbf{x}, \mathbf{p}, t)$ with respect to \mathbf{p} , respectively,

$$c(\mathbf{x}, t) = \int_\Omega \Psi(\mathbf{x}, \mathbf{p}, t) d\mathbf{p}, \quad (6)$$

$$\mathbf{n}(\mathbf{x}, t) = \frac{1}{c(\mathbf{x}, t)} \int_\Omega \Psi(\mathbf{x}, \mathbf{p}, t) \mathbf{p} d\mathbf{p}, \quad (7)$$

$$\mathbf{Q}(\mathbf{x}, t) = \frac{1}{c(\mathbf{x}, t)} \int_\Omega \Psi(\mathbf{x}, \mathbf{p}, t) (\mathbf{p}\mathbf{p} - \mathbf{I}/3) d\mathbf{p}. \quad (8)$$

We also introduce the following quantities, which will become useful in the subsequent analysis:

$$\mathbf{D}(\mathbf{x}, t) = \int_\Omega \Psi(\mathbf{x}, \mathbf{p}, t) (\mathbf{p}\mathbf{p} - \mathbf{I}/3) d\mathbf{p} = c(\mathbf{x}, t) \mathbf{Q}(\mathbf{x}, t), \quad (9)$$

$$\mathbf{S}(\mathbf{x}, t) = \int_\Omega \Psi(\mathbf{x}, \mathbf{p}, t) (\mathbf{p}\mathbf{p}\mathbf{p}\mathbf{p} - \mathbf{l}\mathbf{p}\mathbf{p}/3) d\mathbf{p}. \quad (10)$$

B. Steric interactions

The emergence of collective motion in experiments on bacterial suspensions⁵⁻⁷ typically occurs at such high volume fractions that steric interactions resulting from direct mechanical contacts between particles have a significant impact on particle dynamics. This was clearly noted recently by Cisneros *et al.*,⁷ who observed a transition to local directional order in concentrated suspensions of

swimming *Bacillus subtilis*. The aligning effect of collisions was also reported by Sokolov *et al.*⁵ who observed collisions between pairs of bacteria swimming in two-dimensional stabilized films and found that colliding cells subsequently align and swim as a pair; similar dynamics have also been reported in suspensions of swimming *Paramecia*.³⁶ The importance of steric interactions is also especially clear in swarming experiments with bacterial colonies growing on flat substrates,^{28–30} in which case direct contacts likely even dominate the dynamics as long-ranged hydrodynamic interactions are partially screened by boundaries. In such experiments, local alignment and directionally correlated motion have also been reported to emerge.³⁰

Nematic alignment is well known to arise in concentrated suspensions of Brownian rodlike particles at thermal equilibrium as a result of steric interactions: in these systems, increasing concentration results in a transition from an isotropic to a nematic state by an entropic effect, as the effective volume occupied by a particle in the isotropic phase is larger than in the nematic phase.^{24,37,38} A simple scaling for the critical number density for the transition can be obtained as $n \sim 1/b\ell^2$. This effect is commonly modeled in liquid crystal theories by means of a phenomenological free energy constructed based on symmetry arguments, such as the Landau-de-Gennes free energy^{39,40} which depends quadratically on the nematic order parameter tensor $\mathbf{Q}(\mathbf{x}, t)$ defined in Eq. (8). This approach has also previously been adapted to the case of active liquid crystals^{41,42} and active suspensions,¹⁴ in spite of these systems being out of thermal equilibrium.

A few more sophisticated models for concentrated active suspensions have been posed that are based on a microscopic description of collisions between self-propelled particles. Aranson *et al.*¹³ proposed a continuum model for two-dimensional bacterial suspensions, in which they described steric effects based on a pairwise collision operator having the effect of aligning particles coming into contact. This description, however, relies on the pair probability distribution function in the suspension, which Aranson *et al.* approximated as the product of two singlet distributions. More recently, Baskaran and Marchetti^{43,44} also addressed the effect of collisions in two-dimensional collections of self-propelled hard rods. Using non-equilibrium statistical mechanics, they derived a kinetic theory in which expressions for the translational and orientational fluxes resulting from pairwise collisions were obtained. In particular, they showed that collisions modify the orientational flux by addition of an effective torque captured by the Onsager potential⁴⁵ commonly used in passive liquid crystalline suspensions, but also result in two additional contributions due to the coupling between translational and rotational motions; these contributions have complex forms that depend on the pair distribution function in the suspension and are not easily included in a mean-field model.

In this work, we adopt the classic mean-field treatment of steric interactions motivated by the work of Doi and Edwards^{24,37} on passive suspensions of Brownian rodlike particles, and model the effects of concentration by means of the additional torque in Eq. (5), which is expressed in terms of an interaction potential

$$U(\mathbf{x}, \mathbf{p}, t) = \int_{\Omega} \Psi(\mathbf{x}, \mathbf{p}', t) K(\mathbf{p}, \mathbf{p}') d\mathbf{p}', \quad (11)$$

where the kernel $K(\mathbf{p}, \mathbf{p}')$ describes steric interactions between two slender particles with orientations \mathbf{p} and \mathbf{p}' . In their kinetic theory, Baskaran and Marchetti⁴⁴ showed that an appropriate form is given by the classic Onsager potential:⁴⁵

$$K(\mathbf{p}, \mathbf{p}') = U_0 |\mathbf{p} \times \mathbf{p}'|, \quad (12)$$

which realizes its minimum when \mathbf{p} and \mathbf{p}' are either parallel or anti-parallel. Here, we use the common approximation known as the Maier-Saupe potential:⁴⁶

$$K(\mathbf{p}, \mathbf{p}') = -U_0 (\mathbf{p} \cdot \mathbf{p}')^2, \quad (13)$$

which has the same qualitative effect as the Onsager potential. Note that for Brownian particles, the constant U_0 has a clear thermodynamic origin and can be formally derived based on equilibrium statistical mechanics. In the case of an active suspension where thermal fluctuations are negligible, the parameter U_0 no longer has a clear energetic interpretation but should rather be interpreted as a phenomenological coefficient characterizing the effective magnitude of steric interactions. Its precise value is not easily predicted theoretically but could potentially be obtained using direct

particle simulations such as ours,^{17,18} though these have not yet been applied to the concentrated case of interest here owing to their high computational cost. Such simulations would also serve to verify the expression posited in Eq. (11) for the effective interaction potential.

Substituting Eq. (13) into Eq. (11) immediately yields

$$U(\mathbf{x}, \mathbf{p}, t) = -U_0 \mathbf{p}\mathbf{p} : \mathbf{D}(\mathbf{x}, t) - \frac{U_0}{3} c(\mathbf{x}, t), \quad (14)$$

where $\mathbf{D}(\mathbf{x}, t)$ was defined in Sec. II A. Clearly, we see that the interaction potential $U(\mathbf{x}, \mathbf{p}, t)$ at a given location \mathbf{x} reaches its minimum when \mathbf{p} is aligned with the principal axis of $\mathbf{D}(\mathbf{x}, t)$, which is also the preferred direction of alignment for the swimmers. Using this expression for $U(\mathbf{x}, \mathbf{p}, t)$, Eq. (5) for the angular flux velocity takes on the simple form

$$\dot{\mathbf{p}} = (\mathbf{I} - \mathbf{p}\mathbf{p}) \cdot [\nabla_{\mathbf{x}} \mathbf{u} + 2U_0 \mathbf{D}(\mathbf{x}, t)] \cdot \mathbf{p} - d \nabla_p \ln \Psi. \quad (15)$$

C. Diffusion coefficients

As the analysis of Sec. III will uncover, the rotational and translational diffusions play a central role in the system's stability. Understanding their origins and their dependence on volume fraction and local microstructure is therefore important. Several distinct phenomena can lead to particle diffusion. First, thermal diffusion can be significant in suspensions of artificial microswimmers (such as self-propelled nanorods), though it is typically negligible for biological swimmers. Biological swimmers, however, are still subject to diffusion even in very dilute systems owing to shape imperfections or noise in the swimming actuation.^{47,48} In the absence of interactions, these two effects could be described in terms of constant diffusion coefficients d_0 and D_0 . Note that in the case of a swimming particle, the coupling between rotational diffusion and swimming motion also leads to an additional translational diffusion by an effect similar to generalized Taylor dispersion,⁴⁹ resulting in a net translational diffusivity given by¹⁷ $D = D_0 + V_0^2/6d_0$. At high concentrations, these diffusivities are likely to be affected by steric effects and to depend on the local structure of the suspension. In the case of a passive suspension of rodlike polymers, Doi and Edwards²⁴ suggest that the rotational diffusion in the semi-dilute to concentrated regimes be modeled as

$$d = Cd_0(n\ell^3)^{-2} \left(1 - \frac{3}{2} \mathbf{Q} : \mathbf{Q}\right)^{-1}, \quad (16)$$

and so d depends on the mean volume fraction $n\ell^3$ and local nematic order parameter $\mathbf{Q}(\mathbf{x}, t)$; this particular dependence on volume fraction was recently verified in computer simulations of rigid rods.⁵⁰ Doi and Edwards also predict that the translational diffusivity will become anisotropic, with stronger diffusion in the local direction of alignment (eigenvector of \mathbf{Q} with largest eigenvalue) than in perpendicular directions.

In addition to thermal noise (or noise due to the swimming actuation), semi-dilute and concentrated systems are also subject to hydrodynamic diffusion, which results from fluid-mediated interactions between the particles and can in many cases be the dominant diffusion mechanism. In fairly dilute systems ($n\ell^3 < 1$), a theoretical argument by Subramanian and Koch²³ suggests that $d \propto n\ell^3$, from which $D \propto (n\ell^3)^{-1}$ owing to the Taylor dispersion prediction, and these scalings were indeed verified in our previous particle simulations^{17,18} based on slender-body theory (and which have no imposed stochasticity). The same simulation data, however, also suggest that this dependence may break down at higher concentrations, with d reaching what appears to be a plateau when $n\ell^3 \approx 1$. We are unaware of any numerical simulations of slender swimmers that include hydrodynamic interactions in the concentrated regime, so it is unclear what the dependence on volume fraction becomes beyond this limit.

Because of this multitude of potential diffusion mechanisms, and of the ambiguity of the scaling of the coefficients with volume fraction, we make in this paper the simplest assumption of constant dimensional diffusivities d and D . A more detailed dependence on volume fraction is straightforward to include in the theory, though we do not discuss it further.

D. Mean-field fluid velocity

To close Eqs. (4) and (5) for the flux velocities, the fluid velocity $\mathbf{u}(\mathbf{x})$ generated by the active particles is required. This velocity captures mean-field hydrodynamic interactions between particles, and is driven by the force dipoles that the motile particles exert on the fluid as they propel themselves. In the low-Reynolds-number regime characteristic of microscale swimmers, it can be obtained as a solution of the momentum balance and continuity equation:

$$-\eta \nabla_x^2 \mathbf{u} + \nabla_x q = \nabla_x \cdot \Sigma, \quad \nabla_x \cdot \mathbf{u} = 0, \quad (17)$$

where η is the dynamic viscosity of the suspending Newtonian fluid and q is the pressure. The second-order tensor $\Sigma(\mathbf{x}, t)$ denotes the particle extra stress in the suspension. This particle stress is obtained as a configurational average of the force dipoles exerted by the particles on the fluid.^{51,52} In the case of motile particles,⁵³ it can be decomposed as the sum of four contributions, arising from the permanent dipole due to swimming, Brownian rotations (in the case of colloidal particles), resistance to stretching and compression by the local flow field, and steric torques: $\Sigma = \Sigma^s + \Sigma^b + \Sigma^f + \Sigma^t$.

The first contribution Σ^s due to swimming, corresponding to the active stress, can be modeled as²⁵ $\Sigma^s(\mathbf{x}, t) = \sigma_s \mathbf{D}(\mathbf{x}, t)$. The stress magnitude or dipole strength σ_s depends on the mechanism for swimming and can be of either sign: $\sigma_s > 0$ for head-actuated swimmers, or pullers (such as the microalga *Chlamydomonas reinhardtii*^{54,55}), whereas $\sigma_s < 0$ for rear-actuated swimmers, or pushers (such as the bacteria *Bacillus subtilis* and *Escherichia coli*⁴⁷). From dimensional analysis or from a basic force balance,⁵⁶ it is straightforward to show that $\sigma_s \propto \eta V_0 \ell^2$, where ℓ is the characteristic size of the particles.

The second contribution Σ^b only arises for particles subject to Brownian rotations, and is expressed as⁵⁷ $\Sigma^b(\mathbf{x}, t) = 3kT \mathbf{D}(\mathbf{x}, t)$, where kT is the thermal energy of the solvent. Note that Σ^b has the same tensorial form as Σ^s , and therefore Brownian rotations simply offset the swimming dipole strength σ_s by $3kT$. As most suspensions of motile particles are only weakly affected by Brownian motion, we neglect the Brownian stress in the following discussion, though it can easily be included by modifying the value of σ_s .

The third contribution Σ^f arises because of the assumed inextensibility of the particles, which resist stretching (or compression) by the local fluid flow. This stress tensor was previously calculated for passive particles,^{57,58} and is expressed as $\Sigma^f(\mathbf{x}, t) = \sigma_f \mathbf{S}(\mathbf{x}, t) : \mathbf{E}(\mathbf{x})$, where $\mathbf{E}(\mathbf{x}) = [\nabla_x \mathbf{u} + \nabla_x \mathbf{u}^T]/2$ is the rate-of-strain tensor, and the constant σ_f depends on the shape of the particle. For a slender particle of aspect ratio r , it can be obtained from slender-body theory as $\sigma_f = \pi \eta \ell^3 / 6 \ln(2r)$.

Finally, torques due to local steric interactions also result in a fourth stress contribution, which can be evaluated for a rodlike particle using slender-body theory. We calculate this stress tensor in the Appendix,⁵⁹ where we show that it can be written in the form: $\Sigma^t(\mathbf{x}, t) = -\sigma_t [\mathbf{D}(\mathbf{x}, t) \cdot \mathbf{D}(\mathbf{x}, t) + c(\mathbf{x}, t) \mathbf{D}(\mathbf{x}, t)/3 - \mathbf{S}(\mathbf{x}, t) : \mathbf{D}(\mathbf{x}, t)]$, where for a slender body the constant σ_t can be estimated as $\sigma_t = \pi \eta \ell^3 U_0 / 3 \ln(2r)$. As discussed by Doi and Edwards,²⁴ a similar stress contribution arises in passive suspensions of rodlike particles at thermal equilibrium.

From the form of the various stress tensors, it is straightforward to see that, in dilute suspensions, both Σ^s and Σ^b scale linearly with number density n , whereas Σ^f and Σ^t scale with n^2 in general.⁶⁰ This explains why flow-induced stresses and steric stresses have been neglected in previous work on dilute suspensions.²² However, they cannot be ignored in more concentrated systems such as the ones of interest here. Still, it should be noted that the expressions for the various particle stress tensors used herein remain inherently based on a low-volume-fraction assumption, as they do not include contributions from near-field interactions. In concentrated systems, more complex rheological laws have been derived for the flow-induced stress that account for higher order reflections in the interactions between particles,⁶¹ though these laws are fairly complex and we are unaware of any similar calculation for the steric stress tensor. We therefore focus in this study on the leading-order corrections captured by the expressions derived above, with the caveat that they may not quantitatively capture dependences on volume fraction in very dense systems.

Another assumption of our model, which should be kept in mind, is the one-fluid approximation made when writing the momentum and continuity equations (17). In this model, we assume that

the fluid and particle advection velocities can be described in terms of a single velocity field \mathbf{u} . This assumption, which is equivalent, from the point of view of hydrodynamics, to neglecting the volume of the particles, is again adequate only if the volume fraction is not too high. At high volume fractions, two-fluid models, which have been successfully developed for passive suspensions,^{62–64} would be more appropriate; a first attempt at describing active suspensions in this manner is due to Wolgemuth,¹⁴ though more work remains to be done in this area.

E. Non-dimensionalization

We non-dimensionalize the governing equations using the following characteristic scales for velocities, lengths and times:

$$u_c = V_0, \quad l_c = (n\ell^2)^{-1} = b/v, \quad t_c = l_c/u_c. \quad (18)$$

We also scale the distribution function Ψ with the mean number density n . Upon non-dimensionalization, the conservation equation (1) remains unchanged, but the flux velocities become

$$\dot{\mathbf{x}} = \mathbf{p} + \mathbf{u}(\mathbf{x}) - \nu D^* \nabla_x \ln \Psi, \quad (19)$$

$$\dot{\mathbf{p}} = (\mathbf{I} - \mathbf{p}\mathbf{p}) \cdot [\nabla_x \mathbf{u} + 2U_0^* \mathbf{D}(\mathbf{x}, t)] \cdot \mathbf{p} - \frac{d^*}{\nu} \nabla_p \ln \Psi, \quad (20)$$

where the dimensionless parameters D^* , d^* , and U_0^* are defined as

$$D^* = \frac{D}{bV_0}, \quad d^* = \frac{db}{V_0}, \quad U_0^* = \frac{U_0}{V_0 l^2}. \quad (21)$$

The momentum equation for the fluid velocity simplifies to $-\nabla_x^2 \mathbf{u} + \nabla_x p = \nabla_x \cdot \Sigma$, and the dimensionless particle stress tensor is now expressed as

$$\Sigma(\mathbf{x}, t) = \alpha \mathbf{D} + \beta \nu \mathbf{S} : \mathbf{E} - 2U_0^* \beta \nu \left(\mathbf{D} \cdot \mathbf{D} + \frac{c}{3} \mathbf{D} - \mathbf{S} : \mathbf{D} \right), \quad (22)$$

where the dimensionless coefficients α and β are given by

$$\alpha = \frac{\sigma_s}{\eta V_0 \ell^2}, \quad \beta = \frac{\pi r}{6 \ln(2r)}. \quad (23)$$

In the remainder of the paper, we exclusively use dimensionless variables, and omit asterisks on dimensionless parameters.

III. STABILITY ANALYSES

A. Isotropic and nematic base states

The set of equations described in Sec. II forms a closed system that can be solved for the evolution of the distribution function Ψ in the suspension. Before we study the stability of this system, we first seek steady spatially uniform solutions of the equations of the form $\Psi_0(\mathbf{p})$, which will serve as base states for the linear stability analyses. Such solutions are obtained by setting the angular flux velocity $\dot{\mathbf{p}}$ to zero:

$$\nabla_p \ln \Psi_0 = \xi (\mathbf{I} - \mathbf{p}\mathbf{p}) \cdot \mathbf{D}_0 \cdot \mathbf{p}, \quad (24)$$

where we have defined $\xi = 2U_0 \nu / d$. This equation expresses a balance between angular diffusion and alignment as a result of steric interactions.

An obvious solution of Eq. (24) is given by $\Psi_0 = 1/4\pi$, which corresponds to an isotropic suspension. However, depending on the values of the parameter ξ , we show that this solution may not be unique. We specifically seek orientation distributions that are axisymmetric around a unit vector $\hat{\mathbf{z}}$, which is indeterminate and sets the local preferred direction of alignment. We also define

two additional unit vectors $\hat{\mathbf{x}}$ and $\hat{\mathbf{y}}$ to form an orthonormal basis. In spherical coordinates with polar axis along $\hat{\mathbf{z}}$, we have

$$\mathbf{p} = \cos \phi \sin \theta \hat{\mathbf{x}} + \sin \phi \sin \theta \hat{\mathbf{y}} + \cos \theta \hat{\mathbf{z}}, \quad (25)$$

with $\theta \in [0, \pi]$ and $\phi \in [0, 2\pi)$. We seek axisymmetric distribution functions of the form $\Psi_0(\mathbf{p}) = \Psi_0(\theta)$. For such functions, an easy calculation shows that

$$\mathbf{D}_0 = A[\Psi_0] \left(\hat{\mathbf{z}}\hat{\mathbf{z}} - \frac{\mathbf{I}}{3} \right), \quad (26)$$

where the operator $A[\Psi_0]$ is defined as

$$A[\Psi_0] = \pi \int_0^\pi \Psi_0(\theta) (3 \cos^2 \theta - 1) \sin \theta d\theta. \quad (27)$$

Using Eq. (26), the conservation equation (24) simplifies to

$$\frac{\partial}{\partial \theta} \ln \Psi_0 = -\frac{\xi}{2} \sin 2\theta A[\Psi_0]. \quad (28)$$

This integrates to

$$\Psi_0(\theta) = C \exp \left(\frac{\xi}{4} \cos 2\theta A[\Psi_0] \right), \quad (29)$$

where the integration constant C is determined to normalize Ψ_0 according to Eq. (3). Note that the value of $A[\Psi_0]$ is still unknown. It can be obtained by applying the operator A to Eq. (29), which yields an implicit nonlinear equation. After simplifications, and defining $\delta = A[\Psi_0]\xi/4$, the solution for the orientation distribution is expressed as

$$\Psi_0(\theta) = \frac{\exp(\delta \cos 2\theta)}{2\pi \int_0^\pi \exp(\delta \cos 2\theta') \sin \theta' d\theta'}, \quad (30)$$

where the parameter δ must be a zero of the following function $g(\delta)$:

$$g(\delta) = \delta - \frac{\xi \int_0^\pi \sin \theta (3 \cos^2 \theta - 1) \exp(\delta \cos 2\theta) d\theta}{8 \int_0^\pi \sin \theta \exp(\delta \cos 2\theta) d\theta}. \quad (31)$$

A zero of $g(\delta)$ is clearly obtained when $\delta = 0$ regardless of the value of ξ , and corresponds to the isotropic orientation distribution $\Psi_0 = 1/4\pi$. However, this solution is not unique, and all the zeroes of $g(\delta)$ are plotted in terms of ξ in Fig. 1(a). For low values of ξ (weak steric alignment torque), the isotropic solution is unique (branch 1). However, above the critical value of $\xi_1^c \approx 13.46$, a bifurcation occurs and two additional solutions arise (branches 2 and 3). Both of these correspond to nematic orientation distributions; δ increases with ξ along branch 2, whereas it decreases along branch 3. This third branch even becomes negative when $\xi \geq \xi_2^c = 15$, where it crosses branch 1. Beyond this value, branch 3 corresponds to an orientation distribution in which the particles are laying preferentially in the x - y plane. The orientation distributions for all three branches at $\xi = 20$ are illustrated in Fig. 1(c).

In a physical system, the relevant solution is expected to minimize the total interaction energy, defined as

$$E = \int_\Omega \Psi_0(\mathbf{p}) U(\mathbf{p}) d\mathbf{p} = -U_0 \int_{\Omega'} \int_\Omega \Psi_0(\mathbf{p}) \Psi_0(\mathbf{p}') (\mathbf{p} \cdot \mathbf{p}')^2 d\mathbf{p} d\mathbf{p}', \quad (32)$$

or, for an axisymmetric orientation distribution:

$$E = -2\pi^2 U_0 \int_0^\pi \int_0^\pi \Psi_0(\theta) \Psi_0(\theta') [\sin^2 \theta \sin^2 \theta' + 2 \cos^2 \theta \cos^2 \theta'] \sin \theta \sin \theta' d\theta d\theta'. \quad (33)$$

This energy was calculated along each branch and is plotted in Fig. 1(b). We find that when $\xi \geq \xi_1^c$ the energy minimum is always achieved on branch 2 with the largest value of δ , which corresponds to the nematic orientation distribution with the strongest alignment. In summary, the base-state

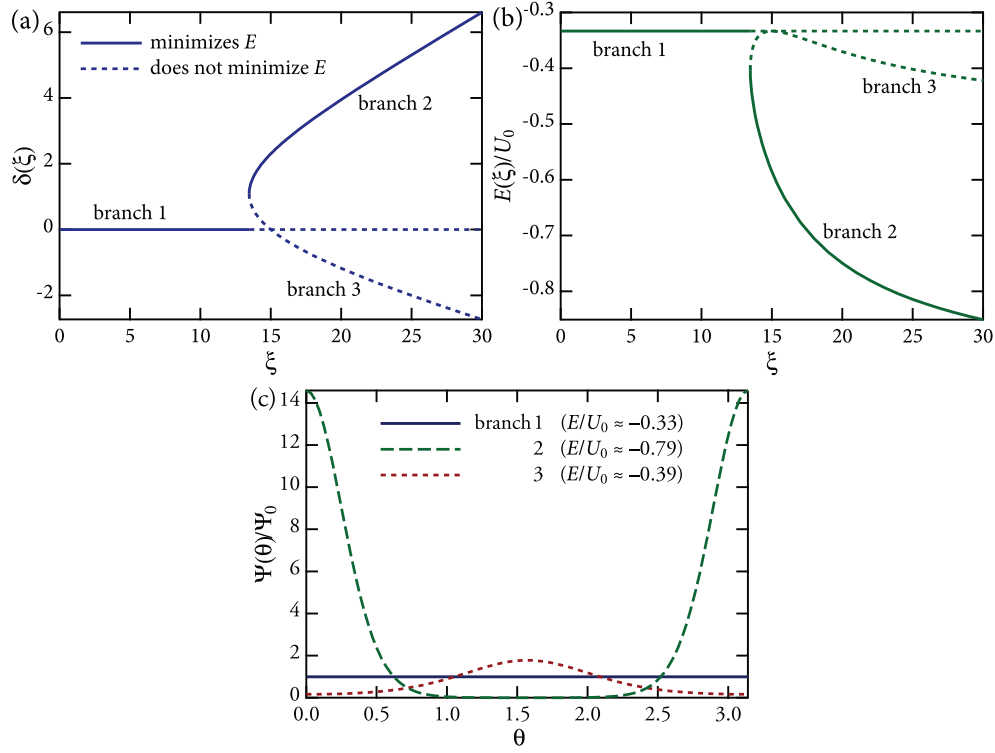


FIG. 1. (a) Solutions of the equation $g(\delta) = 0$, where g is defined in Eq. (31), as functions of $\xi = 2U_0v/d$. Full lines show the branches that, at a given value of ξ , minimize the steric interaction energy. (b) Steric interaction energy $E(\xi)$ along each of the three branches found in (a). (c) Orientation distributions for $\xi = 20$ corresponding to the three solution branches.

orientation distribution is the isotropic one ($\Psi_0 = 1/4\pi$) when $\xi < \xi_1^c \approx 13.46$; above ξ_1^c , the base-state orientation distribution is expected to become nematic and to be given by Eq. (30) where the value for δ should be chosen on branch 2. Note that this discussion is based solely on energy minimization, but does not necessarily reflect the hydrodynamic stability of the various branches, as we describe in more detail below. This was previously noted by Doi and Edwards,²⁴ who also predicted a range of ξ over which both isotropic and nematic phases can exist.

B. Linearized equations and eigenvalue problem

We now proceed to analyze the linear stability of the base states obtained in Sec. III A. We treat the case of an arbitrary base state Ψ_0 , which can be either the isotropic state or a nematic state defined by Eq. (30). We denote by \mathbf{D}_0 and \mathbf{S}_0 the base-state values of the two tensors $\mathbf{D}(\mathbf{x}, t)$ and $\mathbf{S}(\mathbf{x}, t)$. Consider a small perturbation of the distribution function with respect to Ψ_0 :

$$\Psi(\mathbf{x}, \mathbf{p}, t) = \Psi_0(\mathbf{p}) + \epsilon \tilde{\Psi}(\mathbf{x}, \mathbf{p}, t), \quad (34)$$

where $|\epsilon| \ll 1$ and $|\tilde{\Psi}| \sim O(1)$, and similar perturbations are also assumed for the other flow variables. After linearization of the governing equations, the following evolution equation can be obtained for the perturbation:

$$\begin{aligned} \partial_t \tilde{\Psi} + \mathbf{p} \cdot \nabla_x \tilde{\Psi} - \nu D \nabla_x^2 \tilde{\Psi} - \frac{d}{\nu} \nabla_p^2 \tilde{\Psi} + \nabla_p \Psi_0 \cdot (\mathbf{I} - \mathbf{p}\mathbf{p}) \cdot (\nabla_x \tilde{\mathbf{u}} + 2U_0 \tilde{\mathbf{D}}) \cdot \mathbf{p} \\ - 3\Psi_0 \mathbf{p}\mathbf{p} : (\tilde{\mathbf{E}} + 2U_0 \tilde{\mathbf{D}}) + 2U_0 \nabla_p \tilde{\Psi} \cdot (\mathbf{I} - \mathbf{p}\mathbf{p}) \cdot \mathbf{D}_0 \cdot \mathbf{p} - 6U_0 \tilde{\Psi} \mathbf{p}\mathbf{p} : \mathbf{D}_0 = 0. \end{aligned} \quad (35)$$

The perturbation velocity $\tilde{\mathbf{u}}$ satisfies the same momentum equation as \mathbf{u} , but forced by the linearized stress tensor

$$\tilde{\Sigma}(\mathbf{x}, t) = \alpha \tilde{\mathbf{D}} + \beta \nu \mathbf{S}_0 : \tilde{\mathbf{E}} - 2\beta U_0 \nu \left(\mathbf{D}_0 \cdot \tilde{\mathbf{D}} + \tilde{\mathbf{D}} \cdot \mathbf{D}_0 + \frac{1}{3} \tilde{\mathbf{D}} + \frac{\tilde{c}}{3} \mathbf{D}_0 - \mathbf{S}_0 : \tilde{\mathbf{D}} - \tilde{\mathbf{S}} : \mathbf{D}_0 \right). \quad (36)$$

To make analytical progress, we assume that the perturbation can be written as a plane wave with wave vector \mathbf{k} of the form: $\tilde{\Psi}(\mathbf{x}, \mathbf{p}, t) = \hat{\Psi}(\mathbf{p}) \exp(i\mathbf{k} \cdot \mathbf{x} + \sigma t)$, where σ denotes the complex growth rate. In this case, Eq. (35) becomes

$$\begin{aligned} & \sigma \hat{\Psi} + i(\mathbf{p} \cdot \mathbf{k}) \hat{\Psi} + \nu D k^2 \hat{\Psi} - \frac{d}{\nu} \nabla_p^2 \hat{\Psi} + \nabla_p \Psi_0 \cdot (\mathbf{I} - \mathbf{p}\mathbf{p}) \cdot (i\mathbf{k}\hat{\mathbf{u}} + 2U_0 \hat{\mathbf{D}}) \cdot \mathbf{p} \\ & - 3\Psi_0 \mathbf{p}\mathbf{p} : (i\mathbf{k}\hat{\mathbf{u}} + 2U_0 \hat{\mathbf{D}}) \cdot \mathbf{p} + 2U_0 \nabla_p \hat{\Psi} \cdot (\mathbf{I} - \mathbf{p}\mathbf{p}) \cdot \mathbf{D}_0 \cdot \mathbf{p} - 6U_0 \hat{\Psi} \mathbf{p}\mathbf{p} : \mathbf{D}_0 = 0. \end{aligned} \quad (37)$$

Next, we solve for the Fourier component $\hat{\mathbf{u}}$ of the fluid velocity. Standard manipulations⁶⁵ on the continuity and momentum equations yield

$$\hat{\mathbf{u}} = \frac{i}{k} (\mathbf{I} - \hat{\mathbf{k}}\hat{\mathbf{k}}) \cdot \hat{\Sigma} \cdot \hat{\mathbf{k}}, \quad (38)$$

where $\hat{\mathbf{k}} = \mathbf{k}/k$ denotes the wave direction. One must keep in mind, however, that the particle stress tensor $\hat{\Sigma}$ itself depends on $\hat{\mathbf{u}}$ through the flow-induced stress. Specifically, the linearized stress tensor can be written in Fourier space as

$$\hat{\Sigma} = \beta \nu \mathbf{S}_0 : (i\mathbf{k}\hat{\mathbf{u}}) + \hat{\mathbf{C}}, \quad (39)$$

where the second-order tensor $\hat{\mathbf{C}}$ includes contributions from the active and steric stresses and is independent of $\hat{\mathbf{u}}$:

$$\hat{\mathbf{C}} = \alpha \hat{\mathbf{D}} - 2U_0 \beta \nu \left(\mathbf{D}_0 \cdot \hat{\mathbf{D}} + \hat{\mathbf{D}} \cdot \mathbf{D}_0 + \frac{1}{3} \hat{\mathbf{D}} + \frac{\hat{c}}{3} \mathbf{D}_0 - \mathbf{S}_0 : \hat{\mathbf{D}} - \hat{\mathbf{S}} : \mathbf{D}_0 \right). \quad (40)$$

In index notation, Eq. (38) can therefore be written

$$\hat{u}_i = \frac{i}{k} (\delta_{ij} - \hat{k}_i \hat{k}_j) (i\beta \nu S_{ijkl}^0 k_l \hat{u}_m + \hat{C}_{jk}) \hat{k}_k, \quad (41)$$

from which

$$[\delta_{im} + \beta \nu (\delta_{ij} - \hat{k}_i \hat{k}_j) S_{ijkl}^0 \hat{k}_l \hat{k}_k] \hat{u}_m = \frac{i}{k} (\delta_{ij} - \hat{k}_i \hat{k}_j) \hat{C}_{jk} \hat{k}_k. \quad (42)$$

We define the second-order tensor \mathbf{H} as

$$H_{im} = \delta_{im} + \beta \nu (\delta_{ij} - \hat{k}_i \hat{k}_j) S_{ijkl}^0 \hat{k}_k \hat{k}_l. \quad (43)$$

Inverting Eq. (42) for the velocity then yields the solution:

$$\hat{\mathbf{u}} = \frac{i}{k} \mathbf{H}^{-1} \cdot (\mathbf{I} - \hat{\mathbf{k}}\hat{\mathbf{k}}) \cdot \hat{\mathbf{C}} \cdot \hat{\mathbf{k}} = \frac{i}{k} \mathbf{G} : \hat{\mathbf{C}}, \quad (44)$$

where we have introduced a third-order tensor $\mathbf{G} = \mathbf{H}^{-1} \cdot (\mathbf{I} - \hat{\mathbf{k}}\hat{\mathbf{k}}) \hat{\mathbf{k}}$. Equation (44) can be substituted into the linearized equation (37):

$$\begin{aligned} & (\sigma + \nu D k^2) \hat{\Psi} + (i\mathbf{p} \cdot \mathbf{k} - 6U_0 \mathbf{p}\mathbf{p} : \mathbf{D}_0) \hat{\Psi} - \frac{d}{\nu} \nabla_p^2 \hat{\Psi} + \nabla_p \Psi_0 \cdot (\mathbf{I} - \mathbf{p}\mathbf{p}) \cdot (-\hat{\mathbf{k}}\mathbf{G} : \hat{\mathbf{C}} + 2U_0 \hat{\mathbf{D}}) \cdot \mathbf{p} \\ & - 3\Psi_0 \mathbf{p}\mathbf{p} : (-\hat{\mathbf{k}}\mathbf{G} : \hat{\mathbf{C}} + 2U_0 \hat{\mathbf{D}}) + 2U_0 \nabla_p \hat{\Psi} \cdot (\mathbf{I} - \mathbf{p}\mathbf{p}) \cdot \mathbf{D}_0 \cdot \mathbf{p}. \end{aligned} \quad (45)$$

Noting that the only effect of the translational diffusivity D is simply to modify the growth rate by an amount of $-\nu D k^2$, we define a reduced growth rate $\lambda = \sigma + \nu D k^2$, which allows us to write Eq. (45) in the form of an eigenvalue problem with eigenvalue λ :

$$\mathcal{L}[\hat{\Psi}] = \lambda \hat{\Psi}, \quad (46)$$

where \mathcal{L} is a linear integro-differential operator on the unit sphere of orientations defined as

$$\begin{aligned} \mathcal{L}[\hat{\Psi}] = & -(i\mathbf{p} \cdot \mathbf{k} - 6U_0\mathbf{pp} : \mathbf{D}_0)\hat{\Psi} + \frac{d}{v}\nabla_p^2\hat{\Psi} - \nabla_p\Psi_0 \cdot (\mathbf{I} - \mathbf{pp}) \cdot (-\hat{\mathbf{k}}\mathbf{G} : \hat{\mathbf{C}} + 2U_0\hat{\mathbf{D}}) \cdot \mathbf{p} \\ & + 3\Psi_0\mathbf{pp} : (-\hat{\mathbf{k}}\mathbf{G} : \hat{\mathbf{C}} + 2U_0\hat{\mathbf{D}}) - 2U_0\nabla_p\hat{\Psi} \cdot (\mathbf{I} - \mathbf{pp}) \cdot \mathbf{D}_0 \cdot \mathbf{p}. \end{aligned} \quad (47)$$

Recalling that, for the base states derived in Sec. III A, we have

$$\mathbf{D}_0 = \frac{4\delta}{\xi} \left(\hat{\mathbf{z}}\hat{\mathbf{z}} - \frac{\mathbf{I}}{3} \right), \quad \nabla_p\Psi_0 = \frac{\partial\Psi_0}{\partial\theta}\hat{\Theta} = -2\delta\sin 2\theta\Psi_0\hat{\Theta}, \quad (48)$$

where $\hat{\Theta} = \cos\theta\cos\phi\hat{\mathbf{x}} + \cos\theta\sin\phi\hat{\mathbf{y}} - \sin\theta\hat{\mathbf{z}}$ is a unit vector in the θ direction, the expression for \mathcal{L} can be further simplified to

$$\begin{aligned} \mathcal{L}[\hat{\Psi}] = & - \left[i\mathbf{p} \cdot \mathbf{k} - 12\delta\frac{d}{v} \left(\cos^2\theta - \frac{1}{3} \right) \right] \hat{\Psi} + \frac{d}{v}\nabla_p^2\hat{\Psi} \\ & + \Psi_0(2\delta\sin 2\theta\hat{\Theta} + 3\mathbf{p}) \cdot (-\hat{\mathbf{k}}\mathbf{G} : \hat{\mathbf{C}} + 2U_0\hat{\mathbf{D}}) \cdot \mathbf{p} + 2\delta\frac{d}{v}\sin 2\theta\frac{\partial\hat{\Psi}}{\partial\theta}. \end{aligned} \quad (49)$$

Based on the form of Eq. (49), we see that the stability is governed by several dimensionless parameters. In the absence of steric interactions ($U_0 \rightarrow 0$), the only parameters are the dimensionless rotational diffusivity d/v (or, in terms of dimensional variables, $d/nV_0\ell^2$), and the dimensionless active stresslet $\alpha = \sigma_s/\eta V_0\ell^2$, which enters the tensor $\hat{\mathbf{C}}$. When steric interactions are included, additional dimensionless parameters are U_0 (or, in terms of dimensional variables, $U_0/V_0\ell^2$) and $v = nbl^2$, which together uniquely determine δ on any given branch of the base-state solution, and the shape parameter β multiplying the flow-induced and steric stresses.

C. Stability of the isotropic base state

1. Eigenvalue problem

We first study the stability of the uniform isotropic base state, for which the distribution function is given by $\Psi_0 = 1/4\pi$. This is the case that was considered in our previous study in the dilute limit,^{21,22} where we uncovered a long-wavelength linear instability in suspensions of pushers that causes the particles to locally align as a result of hydrodynamic interactions. We expect the steric alignment torque to reinforce this effect, and possibly lead to a similar instability in suspensions of pullers. When $\Psi_0 = 1/4\pi$, the eigenvalue problem [Eq. (46)] simplifies greatly. We first note that $\mathbf{D}_0 = \mathbf{0}$ and that \mathbf{S}_0 is given in index notation by

$$S_{ijkl}^0 = \frac{1}{15} \left[\delta_{ik}\delta_{jl} + \delta_{il}\delta_{jk} - \frac{2}{3}\delta_{ij}\delta_{kl} \right]. \quad (50)$$

The tensor $\hat{\mathbf{C}}$ defined in Eq. (40) can also be calculated as

$$\hat{C}_{ij} = \alpha\hat{D}_{ij} - 2U_0\beta v \left[\frac{1}{3}\hat{D}_{ij} - S_{ijkl}^0\hat{D}_{kl} \right] = \left(\alpha - \frac{2}{5}U_0\beta v \right) \hat{D}_{ij}, \quad (51)$$

where we have used the symmetry and tracelessness of $\hat{\mathbf{D}}$. The tensor \mathbf{H} and its inverse can then be obtained as

$$\mathbf{H} = \left(1 + \frac{\beta v}{15} \right) \mathbf{I} - \frac{\beta v}{15} \hat{\mathbf{k}}\hat{\mathbf{k}}, \quad \mathbf{H}^{-1} = \left(1 + \frac{\beta v}{15} \right)^{-1} \left(\mathbf{I} + \frac{\beta v}{15} \hat{\mathbf{k}}\hat{\mathbf{k}} \right), \quad (52)$$

from which we easily find that

$$\mathbf{G} : \hat{\mathbf{C}} = \frac{\alpha - \frac{2}{5}U_0\beta v}{1 + \frac{\beta v}{15}} (\mathbf{I} - \hat{\mathbf{k}}\hat{\mathbf{k}}) \cdot \hat{\mathbf{D}} \cdot \hat{\mathbf{k}} \equiv \bar{\alpha}(v) (\mathbf{I} - \hat{\mathbf{k}}\hat{\mathbf{k}}) \cdot \hat{\mathbf{D}} \cdot \hat{\mathbf{k}}. \quad (53)$$

We have introduced the notation $\bar{\alpha}(v)$ for the prefactor:

$$\bar{\alpha}(v) = \frac{\alpha - \frac{2}{5}U_0\beta v}{1 + \frac{\beta v}{15}}, \quad (54)$$

which has an easy physical interpretation. In the dilute limit $v \rightarrow 0$, it is simply given by α , which is the dimensionless active dipole strength. Here, we find that interactions modify this dipole strength in two ways. First, the steric stress decreases the value of α by $-2U_0\beta v/5$, i.e., has a destabilizing effect since dilute suspensions are unstable for $\alpha < 0$ (pushers). Second, the denominator in Eq. (54) can be interpreted as the dimensionless viscosity in an isotropic suspension: $1 + \beta v/15 = 1 + \pi n \ell^3/6 \ln(2r)$; flow-induced stresses are seen to result in a viscosity increase, which is linear in volume fraction and stabilizes the system (in the case of pushers) by effectively decreasing the magnitude of the active dipole strength.

Using Eq. (52), we simplify Eq. (47) for the operator \mathcal{L} to

$$\mathcal{L}[\hat{\Psi}] = -i(\mathbf{p} \cdot \mathbf{k})\hat{\Psi} + \frac{d}{v}\nabla_p^2\hat{\Psi} - \frac{3\bar{\alpha}(v)}{4\pi}(\mathbf{p} \cdot \mathbf{k})[\mathbf{p} \cdot (\mathbf{I} - \hat{\mathbf{k}}\hat{\mathbf{k}}) \cdot \hat{\mathbf{D}} \cdot \hat{\mathbf{k}}] + \frac{6}{4\pi}U_0\mathbf{p}\mathbf{p} : \hat{\mathbf{D}}. \quad (55)$$

The four terms in $\mathcal{L}[\hat{\Psi}]$ originate from transport by the swimming velocity, rotational diffusion, alignment in the hydrodynamic flow driven by active and steric stresses, and alignment under the steric torque, respectively.

2. Spherical harmonic expansion

We solve the eigenvalue problem of Eq. (46) spectrally using an expansion of the eigenfunction $\hat{\Psi}(\mathbf{p})$ on the basis of spherical harmonics. We choose a spherical coordinate system in which \mathbf{k} is aligned with the polar axis. Denoting by $\theta \in [0, \pi]$ and $\phi \in [0, 2\pi)$ the polar and azimuthal angles, respectively, we have

$$\hat{\mathbf{k}} = [0, 0, 1], \quad \text{and} \quad \mathbf{p} = [\sin \theta \cos \phi, \sin \theta \sin \phi, \cos \theta]. \quad (56)$$

In this coordinate system, the spherical harmonic of degree ℓ and order $m = -\ell, \dots, \ell$ is defined as

$$\mathcal{Y}_\ell^m(\theta, \phi) = \sqrt{\frac{2\ell + 1}{4\pi} \frac{(\ell - m)!}{(\ell + m)!}} P_\ell^m(\cos \theta) \exp im\phi \quad (57)$$

in terms of the associated Legendre polynomial $P_\ell^m(\cos \theta)$. The spherical harmonics satisfy the orthogonality condition:

$$\langle \mathcal{Y}_\ell^m, \mathcal{Y}_{\ell'}^{m'} \rangle = \int_{\phi=0}^{2\pi} \int_{\theta=0}^{\pi} \mathcal{Y}_\ell^m(\theta, \phi) \mathcal{Y}_{\ell'}^{m'*}(\theta, \phi) \sin \theta d\theta d\phi = \delta_{\ell, \ell'} \delta_{m, m'}, \quad (58)$$

where $*$ denotes the complex conjugate. These functions form a complete basis on the unit sphere Ω , on which we expand the mode shape $\hat{\Psi}$ as

$$\hat{\Psi}(\theta, \phi) = \sum_{\ell=0}^{\infty} \sum_{m=-\ell}^{\ell} \psi_\ell^m(\mathbf{k}) \mathcal{Y}_\ell^m(\theta, \phi). \quad (59)$$

After substituting Eq. (59) into Eq. (46) and applying orthogonality, the eigenvalue problem for the mode shape becomes an algebraic eigenvalue problem for the harmonic amplitudes:

$$\sum_{\ell'=0}^{\infty} \sum_{m'=-\ell'}^{\ell'} L_{\ell m}^{\ell' m'} \psi_{\ell'}^{m'} = \lambda \psi_\ell^m, \quad (60)$$

where the coefficients $L_{\ell m}^{\ell' m'}$ are defined as $L_{\ell m}^{\ell' m'} = \langle \mathcal{L}[\mathcal{Y}_\ell^m], \mathcal{Y}_{\ell'}^{m'} \rangle$. These can be obtained analytically as

$$\begin{aligned} L_{\ell m}^{\ell' m'} = & -ik[A_{\ell'}^{m'} \delta_{\ell, \ell'+1} + B_{\ell'}^{m'} \delta_{\ell, \ell'-1}] \delta_{m, m'} - \frac{d}{v} \ell(\ell+1) \delta_{\ell, \ell'} \delta_{m, m'} \\ & + [4U_0/5 - \bar{\alpha}(v)/5] (\delta_{\ell, 2} \delta_{\ell, \ell'} \delta_{m, -1} \delta_{m, m'} + \delta_{\ell, 2} \delta_{\ell, \ell'} \delta_{m, 1} \delta_{m, m'}) \\ & + [4U_0/5] (\delta_{\ell, 2} \delta_{\ell, \ell'} \delta_{m, 0} \delta_{m, m'} + \delta_{\ell, 2} \delta_{\ell, \ell'} \delta_{m, -2} \delta_{m, m'} + \delta_{\ell, 2} \delta_{\ell, \ell'} \delta_{m, 2} \delta_{m, m'}), \end{aligned} \quad (61)$$

where δ is the Kronecker delta and the constants A_ℓ^m and B_ℓ^m are given by

$$A_\ell^m = \sqrt{\frac{(\ell - m + 1)(\ell + m + 1)}{(2\ell + 1)(2\ell + 3)}}, \quad B_\ell^m = \sqrt{\frac{(\ell - m)(\ell + m)}{(2\ell - 1)(2\ell + 1)}}. \quad (62)$$

In particular, inspection of Eq. (61) reveals that spherical harmonics diagonalize the operator \mathcal{L} , with the exception of the first term on the right-hand side of Eq. (55), which expresses transport by the swimming velocity. We also observe that sets of equations corresponding to different values of the order m are uncoupled and can therefore be solved separately. The only orders that can be subject to instabilities are $m = 0, 1, 2$ (as well as $m = -1, -2$, which are identical to $m = 1, 2$); other orders only undergo transport by the swimming velocity and damping by rotational diffusion.

In the long-wave limit of $k \rightarrow 0$, analytical solutions for the growth rates corresponding to modes of a given order m can be obtained. To each value of m is associated a discrete infinite spectrum with countable eigenvalues:

$$m = 0: \quad \lambda_\ell^m = 4U_0/5 \delta_{\ell, 2} - \frac{d}{v} \ell(\ell + 1), \quad (63)$$

$$m = 1: \quad \lambda_\ell^m = [4U_0/5 - \bar{\alpha}(v)/5] \delta_{\ell, 2} - \frac{d}{v} \ell(\ell + 1), \quad (64)$$

$$m = 2: \quad \lambda_\ell^m = 4U_0/5 \delta_{\ell, 2} - \frac{d}{v} \ell(\ell + 1), \quad (65)$$

$$m \geq 3: \quad \lambda_\ell^m = -\frac{d}{v} \ell(\ell + 1), \quad (66)$$

where the degree $\ell \geq m$ is a positive integer. In the limit of $k = 0$, the corresponding eigenfunctions (or mode shapes) are simply the spherical harmonics, and therefore form a complete set. Note that when k is strictly zero (spatially homogeneous suspension), the active term involving α in Eq. (64) should technically be discarded as there is no hydrodynamic flow in this limit. We find that modes $m = 0$ and 2 are unaffected by hydrodynamics, and become unstable for $\ell = 2$ provided that

$$\frac{4U_0}{5} - \frac{6d}{v} > 0, \quad \text{i.e.,} \quad \xi = \frac{2U_0 v}{d} > \xi_2^c = 15. \quad (67)$$

In Fig. 1(a), this corresponds to the intersection of branch 1 (isotropic base state), with branch 3, where we expect an exchange of stability to take place. Above this value of ξ , the isotropic base state is always unstable in the long-wave limit for both pushers and pullers, purely as a result of steric interactions.

The stability of mode $m = 1$ is more complex as it is also affected by hydrodynamics. We find that this mode becomes unstable for $\ell = 2$ if

$$\frac{\xi}{15} \left(1 + \frac{\beta v / 10}{1 + \frac{1}{15} \beta v} \right) - \frac{\alpha v / 30 d}{1 + \frac{1}{15} \beta v} > 1. \quad (68)$$

We see that steric interactions tend to destabilize this mode via the first term in Eq. (68), whereas active stresses are stabilizing in the case of pullers ($\alpha > 0$) and destabilizing in the case of pushers ($\alpha < 0$), in agreement with the dilute theory.²¹ Both effects are modulated by the effective volume fraction v , through both steric and flow-induced (viscous) stresses. The marginal stability curve in the $(v, \alpha v / 30 d)$ plane (in the limit of $k \rightarrow 0$) is shown in Fig. 2 for various values of $2U_0/d$. In the

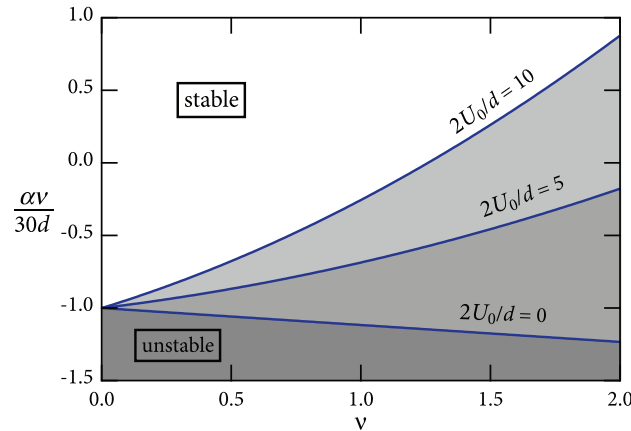


FIG. 2. Marginal stability curve in the long-wave limit ($k \rightarrow 0$) in terms of effective volume fraction ν and dimensionless dipole strength $\alpha\nu/30d$, for various values of $2U_0/d$ [see Eq. (68)]. In this plot, $\beta = 1.75$, corresponding to a particle aspect ratio of $r \approx 10$.

dilute limit ($\nu \rightarrow 0$), all curves converge to $\alpha\nu/30d = -1$, which corresponds to the critical dipole strength below which dilute pusher suspensions are subject to instabilities as $k \rightarrow 0$.²⁶ If steric interactions are neglected ($2U_0/d = 0$), increasing ν results in a decrease of this critical strength as a result of the increased effective viscosity of the suspension. However, when steric interactions are present ($2U_0/d > 0$), both the steric torque and steric stresses have a destabilizing effect and increase the critical value of $\alpha\nu/30d$, which even becomes positive at sufficiently large values of ν , i.e., both pusher and puller suspensions can be subject to instabilities.

At finite wavenumber (arbitrary value of $k > 0$), the growth rates can no longer be obtained analytically, but they can be calculated numerically by solving the algebraic eigenvalue problem Eq. (60) for each value of m , after truncation of the infinite sum at a finite degree ℓ chosen large enough to ensure convergence of the dominant eigenvalues. Numerical solutions for the real and imaginary parts of λ for modes $m = 0, 1, 2$ are shown in Fig. 3 for different values of $\xi = 2U_0\nu/d$, where only the first few eigenvalues with the largest real parts (or growth rates) are plotted. As ξ increases, some of these growth rates become positive as all three modes become unstable above a critical value ξ^c . The largest growth rates are always found to occur at $k = 0$ (infinite wavelength), and finite-wavelength interactions between the spherical harmonics lead to damping at high wavenumbers. In agreement with the long-wave analysis, modes $m = 0$ and 2 become unstable above $\xi^c = \xi_2^c = 15$; however, pullers ($\alpha > 0$) tend to stabilize mode $m = 1$ ($\xi^c > \xi_2^c$), whereas pushers ($\alpha < 0$) further destabilize it ($\xi^c < \xi_2^c$) as shown in Fig. 3(b). Figure 4 also shows the range of unstable wavenumbers as a function of ξ for all three modes. In all three cases, the unstable range tends to a finite interval of the form $[0, k_c]$ as $\xi \rightarrow \infty$, where k_c is of order $O(1)$ [or, in dimensional units, $O(n\ell^2)$], and where the largest growth rate always occurs for $k = 0$.

D. Stability of the nematic base states

We now turn our attention to the stability of the nematic base state of Eq. (30), for which the coefficients $L_{\ell m}^{\ell' m'}$ in the algebraic eigenvalue problem of Eq. (60) can no longer be calculated analytically. Indeed, it can be seen that the operator \mathcal{L} still only involves azimuthal modes $m = -2, -1, 0, 1, 2$, but now has a complex dependence on the polar angle θ through the anisotropic base state. The coefficients $L_{\ell m}^{\ell' m'}$ can, however, be calculated numerically, as can the corresponding eigenvalues. A significant number of polar modes have to be included for convergence, and this number is found to increase with ξ . For $\xi \lesssim 30$, we find that 20 polar modes are sufficient. Another notable difference with the isotropic case is the dependence of the eigenvalue problem, and therefore of the stability results, on the direction $\hat{\mathbf{k}}$ of the wave with respect to the base-state alignment direction, which can be characterized by a single angle $\Theta = \cos^{-1}(\hat{\mathbf{k}} \cdot \hat{\mathbf{z}})$.

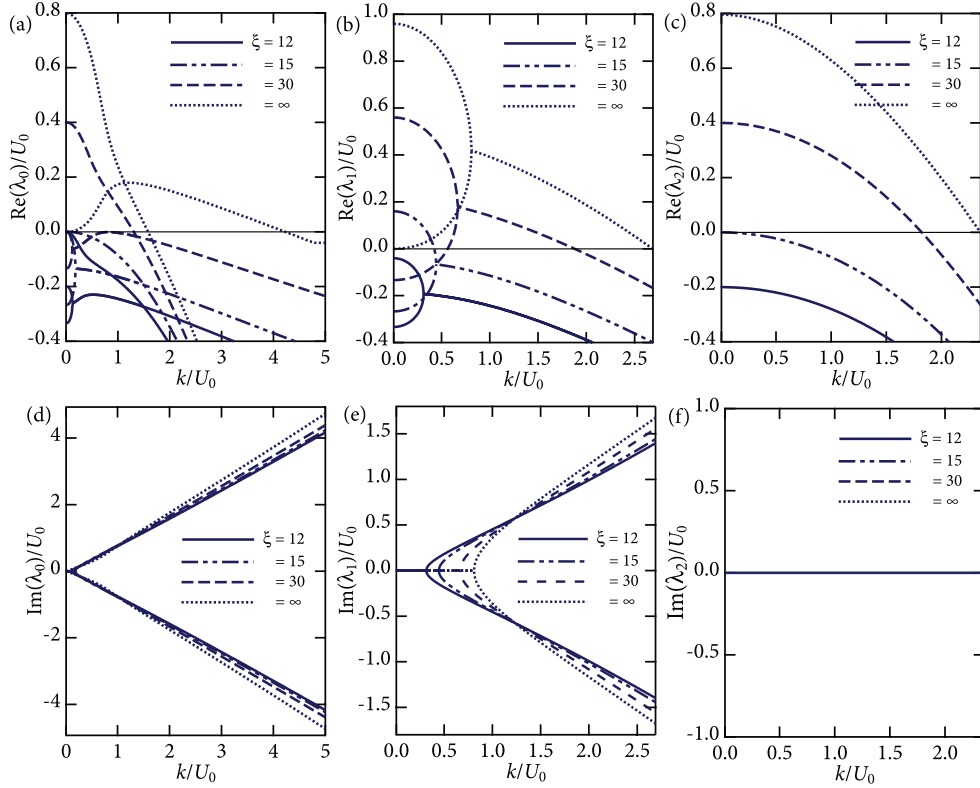


FIG. 3. Numerical solutions of the dispersion relations Eqs. (60) and (61) for the complex growth rates λ_0 , λ_1 , and λ_2 of azimuthal modes $m = 0, 1, 2$ as functions of the wavenumber k . (a)–(c) show the real parts, while (d)–(f) show the imaginary parts. In (b) and (e), we set $\beta = 0$ to isolate the leading-order effect of the steric torque, and $\alpha/4U_0 = -0.2$ (pushers).

In all the results described in this section, we set the rotational diffusivity d and the strength of steric interactions U_0 to the values: $d = 0.002$ and $U_0 = 0.1346$, and focus on the influence of varying the parameter $\xi = 2U_0\nu/d$, which is equivalent to varying the effective volume fraction ν . With this choice of parameters, $\nu = 0.1$ when $\xi = \xi_1^c = 13.46$. We also set the shape parameter β appearing in the particle stress Eq. (22) to $\beta = 1.75$, which corresponds to a particle aspect ratio of $r \approx 10$. These parameter values, which will also be used in the simulations of Sec. IV, were chosen so as to keep the factor $\beta\nu$, which sets the magnitude of the flow-induced and steric stresses, relatively

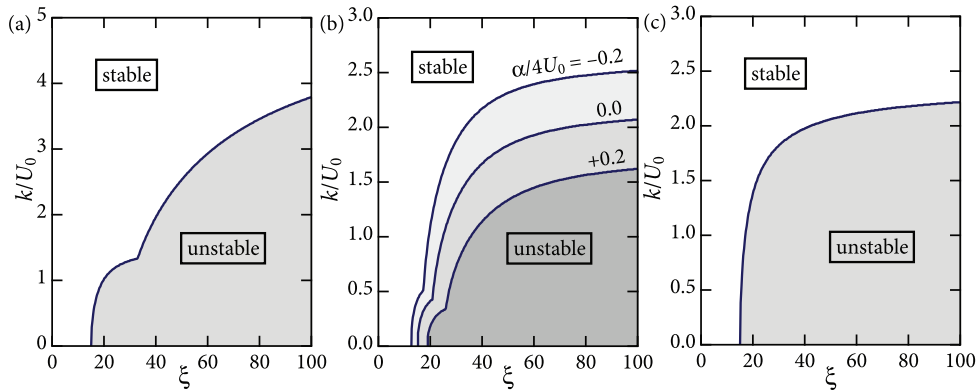


FIG. 4. Unstable range of wavenumbers as a function of $\xi = 2U_0\nu/d$ for azimuthal modes $m = 0$ (a), 1 (b), and 2 (c). For mode 1, we set $\beta = 0$ to isolate the leading-order effect of the steric torque.

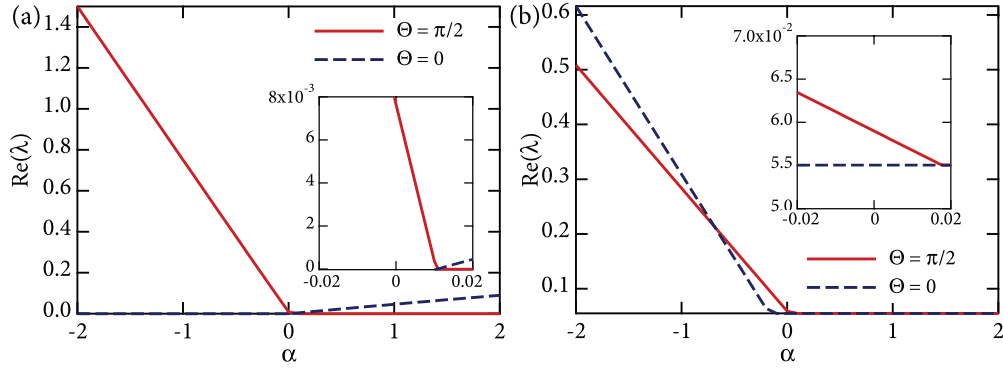


FIG. 5. Dependence of the maximum reduced growth rate $\text{Re}(\lambda)$ governing the stability of the nematic base states on the dimensionless active stress magnitude α , for $\xi = 20$: (a) branch 2 and (b) branch 3. Results for two different wave orientations Θ are shown. Insets show close-ups on the region near the origin.

small. This is motivated by the previous observation that the quadratic dependence of both stress tensors on effective volume fraction is based on a low-volume fraction assumption, see Sec. II D.

We first focus on the long-wave limit of $k \rightarrow 0$, in which case the convective term $-i(\mathbf{p} \cdot \mathbf{k})\hat{\Psi}$ in the definition of \mathcal{L} in Eq. (49) vanishes. Figure 5 show the dependence of the maximum real part of the eigenvalue λ as a function of dimensionless active stress magnitude α on both nematic branches for $\xi = 20$. Results for two wave orientations Θ are shown. On branch 2 and for this value of ξ [Fig. 5(a)], both pushers and pullers are predicted to be unstable, though for different wave orientations. Branch 3, as shown in Fig. 5(b), is also unstable for all values of α , though it is further destabilized by activity in the case of pushers. We note an interesting dependence of the growth rate on the wave direction Θ : for a given value of α , waves of different orientations have distinct stability properties.

The precise dependence on the parameter ξ is shown in Fig. 6, where the stability of both nematic branches is illustrated for two different wave directions. Figures 6(a) and 6(b) show the

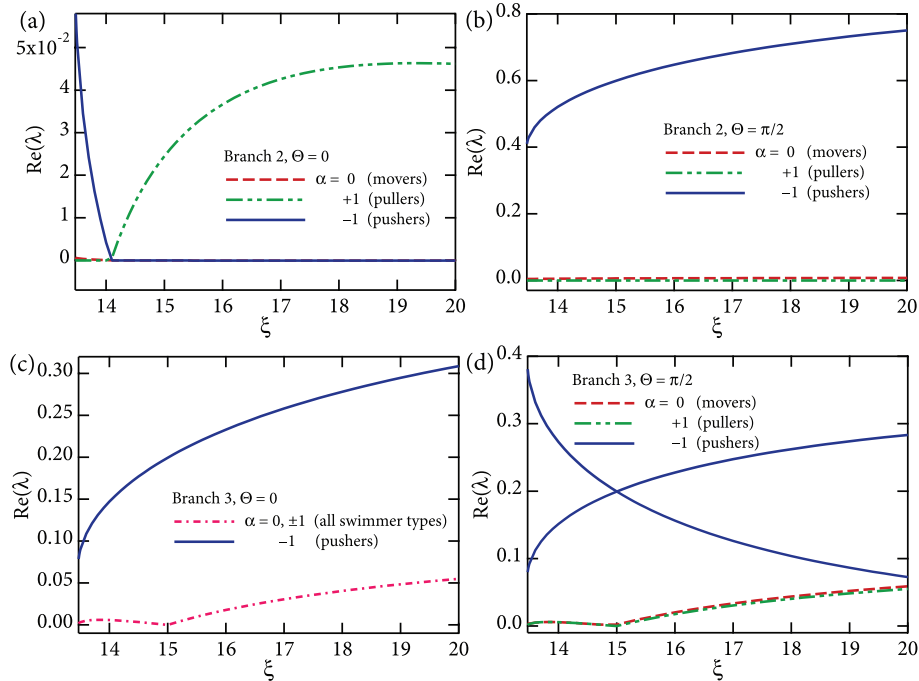


FIG. 6. Dependence of the maximum reduced growth rate $\text{Re}(\lambda)$ on the parameter ξ , along both nematic branches, for two different wave directions Θ : (a) branch 2, $\Theta = 0$; (b) branch 2, $\Theta = \pi/2$; (c) branch 3, $\Theta = 0$; and (d) branch 3, $\Theta = \pi/2$.

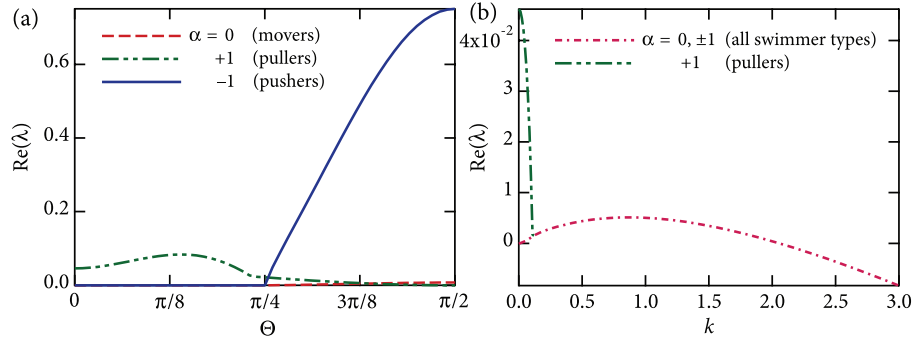


FIG. 7. Dependence of the maximum reduced growth rate $\text{Re}(\lambda)$ on: (a) wave direction Θ (in the limit of $k \rightarrow 0$), and (b) wavenumber k (for a wave with orientation $\Theta = 0$). Both plots were obtained on branch 2, with $\xi = 20$.

stability of branch 2, for $\Theta = 0$ and $\pi/2$, respectively. On this branch, which is the most energetically favorable base state according to the analysis of Sec. III A, we find that pushers ($\alpha = -1$) are always unstable for $\Theta = \pi/2$, though some wave orientations such as $\Theta = 0$ are observed to be stable at high values of ξ . In the case of pullers ($\alpha = +1$), activity has a stabilizing effect for low values of ξ (precisely when $\xi \lesssim 14.1$ for the present choice of parameters), but an instability occurs above this threshold for $\Theta = 0$. The case of movers, which do not exert any active stress, is characterized by a very low but positive growth rate, which is approximately two orders of magnitude smaller than the characteristic growth rate of either pushers or pullers; this weak instability can be shown to be a consequence of the steric stress rather than the active stress, and is observed to disappear when $\beta = 0$. The stability of the other nematic branch (branch 3), which is the least energetically favorable, is illustrated in Figs. 6(c) and 6(d); on this branch, we find that all types of particles exhibit instabilities.

As noted in Figs. 5 and 6, different wave orientations Θ can have different stability characteristics. This is described more precisely in Fig. 7(a), where we plot the maximum growth rate as a function of Θ on branch 2 when $\xi = 20$. In agreement with Fig. 6, we observe a positive growth rate in suspensions of pullers for low values of Θ (with $\Theta = 0$ corresponding to a wave in the direction of particle alignment), whereas pushers and movers are most unstable when $\Theta = \pi/2$ (corresponding to a wave in a direction perpendicular to that of the nematic base state). The precise range of unstable wave directions for a given swimmer type is also observed to depend on the value of ξ .

As in the case of the isotropic branch discussed in Sec. III C, the stability of the nematic branches has a non-trivial dependence on wavenumber k as a result of the convective term $-i(\mathbf{p} \cdot \mathbf{k})\hat{\Psi}$ (arising from the swimming velocity) in the operator \mathcal{L} . This dependence is illustrated in Fig. 7(b) in the case of a wave with direction $\Theta = 0$ at $\xi = 20$ on branch 2. While increasing k can initially destabilize certain eigenmodes, all growth rates are found to decay and eventually become negative at large enough values of k .

E. Summary of stability analyses and stability diagrams

The results of the stability analyses of the various isotropic and nematic base states are summarized in the form of stability diagrams in Fig. 8 for all three types of swimmers:

- *Movers*: The case of movers, which do not drive active stresses but result in flow-induced and steric stresses in addition to being subject to steric alignment torques, is shown in Fig. 8(a). The isotropic base state is found to be stable when $\xi < \xi_2^c = 15$, and unstable for higher values of ξ . The two nematic base states have distinct stability characteristics. Branch 3, which is the least favorable energetically as discussed in Sec. III A, is always unstable. Branch 2, in the long-wave limit, is subject of a weak instability with a very small growth rate. This instability is due solely to the steric stress and vanishes when $\beta = 0$; as will be discussed in Sec. IV, it is not observed in our simulations, where it is likely suppressed by the finite box size and

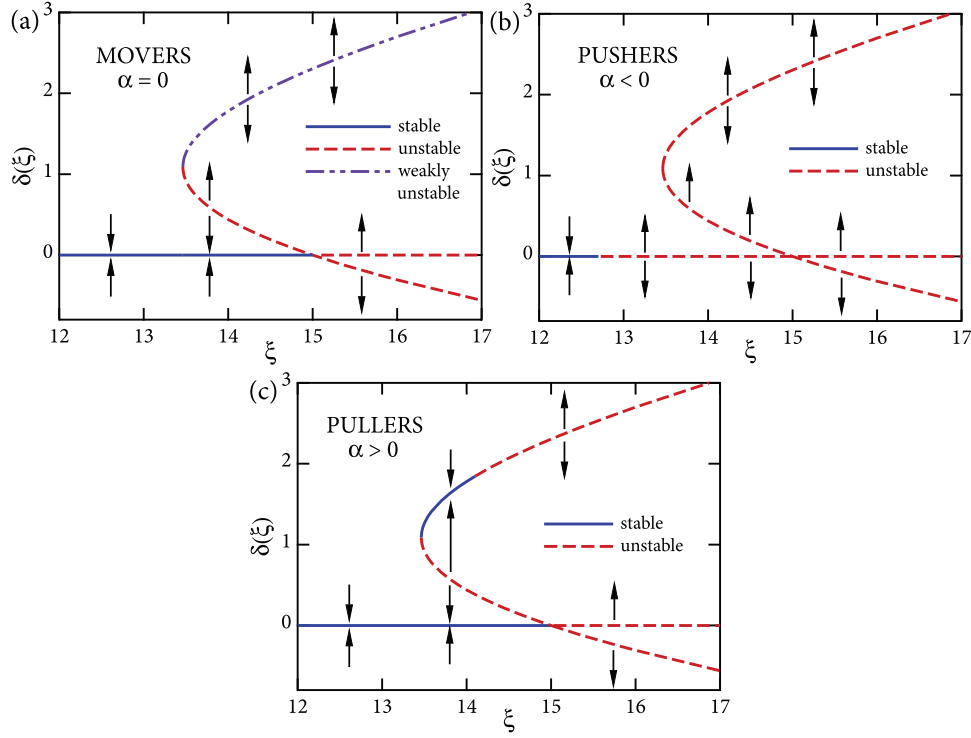


FIG. 8. Stability diagrams for: (a) movers ($\alpha = 0$), (b) pushers ($\alpha < 0$), and (c) pullers ($\alpha > 0$). A branch is labeled unstable if there exists a positive growth rate $\text{Re}(\lambda) > 0$. In the case of movers, branch 2 is only weakly unstable, as the growth rates on that branch are very low (two orders of magnitude lower than on other unstable branches).

translational diffusion. If the instability of branch 2 does not occur, we therefore find that there exists a finite range $\xi \in [\xi_1^c, \xi_2^c]$ over which both isotropic and nematic base states are hydrodynamically stable (even though the nematic state of branch 2 realizes a lower minimum of the steric interaction energy). This was previously noted by Doi and Edwards,²⁴ and suggests the existence of a hysteresis loop with possible phase separation near the isotropic-to-nematic transition.

- *Pushers*: The stability diagram for pushers, which also exert active stresses with $\alpha < 0$, is shown in Fig. 8(b). In this case, the isotropic case is found to become unstable above a critical value ξ^c that can be obtained from Eq. (64) as

$$\xi^c = 15 + \frac{v\bar{\alpha}(v)}{2d} = 15 + \frac{v}{2d} \left(\frac{\alpha - \frac{2}{5}U_0\beta v}{1 + \frac{\beta v}{15}} \right). \quad (69)$$

Because $\alpha < 0$, it is clear that $\xi^c < \xi_2^c = 15$, i.e., the isotropic base state becomes hydrodynamically unstable before the isotropic-to-nematic transition. In the case where $\beta v \ll 1$ and $U_0 = 0$ (dilute limit with no steric interactions), Eq. (69) reduces to the dilute marginal stability condition on α in the presence of rotational diffusion. The existence of an instability in the isotropic base state is not a surprising result in the light of our previous analysis of dilute suspensions, which were found to be always unstable in the case of pushers in the long-wave limit when diffusion was neglected.^{21,22} Rotational diffusion, however, can stabilize pusher suspensions at low values of ξ , which correspond to very low volume fractions or large values of d . This effect was previously noted by Subramanian and Koch²³ and Hohenegger and Shelley.²⁶ In the nematic regime, both branches 2 and 3 are found to be always unstable, at least over a certain range of the wave angle Θ . Pusher suspensions are therefore always expected to undergo unsteady chaotic dynamics when $\xi > \xi^c$; this is indeed confirmed by our simulations in Sec. IV.

- *Pullers*: In the case of pullers, active stresses also arise (with $\alpha > 0$) but are known to have a stabilizing effect in dilute suspensions.^{21,22} As shown in Fig. 8(c), the isotropic case becomes unstable when ξ reaches $\xi_2^c = 15$, as in the case of movers; the instability that occurs above this value is solely due to steric effects, first through azimuthal modes $m = 0$, and 2, and finally through mode $m = 1$, which is stabilized by activity up to a higher value of ξ (Sec. III C). The nematic state of branch 3, as in the case of movers, is found to always be unstable. The effect of activity is seen most clearly on the nematic base state of branch 2, which is stable over a finite range of values of ξ just above $\xi_1^c \approx 13.46$, but becomes unstable at larger values of ξ . This differs fundamentally from the dilute case where isotropic puller suspensions are always predicted to be stable; however, the observation that nematic suspensions of either pullers or pushers are unstable at large values of ξ is perhaps unsurprising based on our previous analysis of aligned suspensions, which had assumed perfect alignment and negligible rotational diffusion,^{21,22} and on our previous simulations of aligned suspensions, which were found to always become unstable.¹⁷ As in the case of movers, there can exist a range of values of ξ near the isotropic-to-nematic transition where both isotropic and nematic base states are hydrodynamically stable, possibly leading to hysteresis and phase separation.

One should keep in mind that the stability results obtained above all pertain to the reduced growth rate $\lambda = \sigma + \nu Dk^2$, and that translational diffusion D can therefore stabilize all branches, particularly at high wavenumbers. Also recall that all branches that are unstable as $k \rightarrow 0$ become stable at sufficiently large values of k even in the absence of translational diffusion, as a result of convection by the swimming velocity.

IV. NUMERICAL SIMULATIONS

A. Simulation method and parameter selection

We complement the linear stability analyses of Sec. III by performing fully nonlinear simulations of the kinetic model of Sec. II in a periodic domain. The numerical method used is a direct extension of the work of Alizadeh Pahlavan and Saintillan,²⁷ and is based on a finite-difference solution of the Smoluchowski equation (1) using second-order central finite differences in space and orientation and a second-order Adams-Bashforth time-integration scheme. A spectral solution of the Stokes equations is used, in which we use a three-point extrapolation scheme to evaluate the flow-induced stresses (which depend on the velocity gradient) at the current time step in terms of the two previous time steps. We use a total of 64^3 discretization points for the x , y , and z spatial coordinates, and 16^2 points for the θ and ϕ angular coordinates, which parameterize the orientation vector \mathbf{p} as in Eq. (56). Simulations were typically run using a 64-processor parallel computer.

All simulations shown were performed in a periodic cubic box with linear dimension $L/l_c = 50$. The particle translational and rotational diffusion coefficients are set to $D = 2.0$ and $d = 0.002$, and the dimensionless strength of steric interactions is set to $U_0 = 0.1346$, so that $\xi = \xi_1^c = 13.46$ is reached when $\nu = 0.1$; these values of d and U_0 are identical to those used in the stability analysis of the nematic base states in Sec. III D. Swimming particles are assumed to have an aspect ratio of $r = 10$, from which the parameter β appearing in the magnitude of the flow-induced and steric stress tensors is given by $\beta = 1.75$. Finally, we present results for two values of the dimensionless active stress: $\alpha = -1$ (pushers), and $\alpha = +1$ (pullers). Simulations of movers ($\alpha = 0$) never evolved towards unsteady states and either converged to the isotropic or nematic base states depending on the value of ξ . In particular, we were never able to observe the weak instability of branch 2 predicted by the stability analysis; this discrepancy is likely a consequence of the finite size of the domain in the simulations, and of translational diffusion. A few simulations of shakers, which are particles that do not swim ($V_0 = 0$) but exert an active stress ($\alpha = \pm 1$) are also discussed. Several values of the effective volume fraction ν are considered, so as to explore the various regimes highlighted in the stability diagrams of Fig. 8. In all simulations, the initial condition is uniform and isotropic with a weak random perturbation.

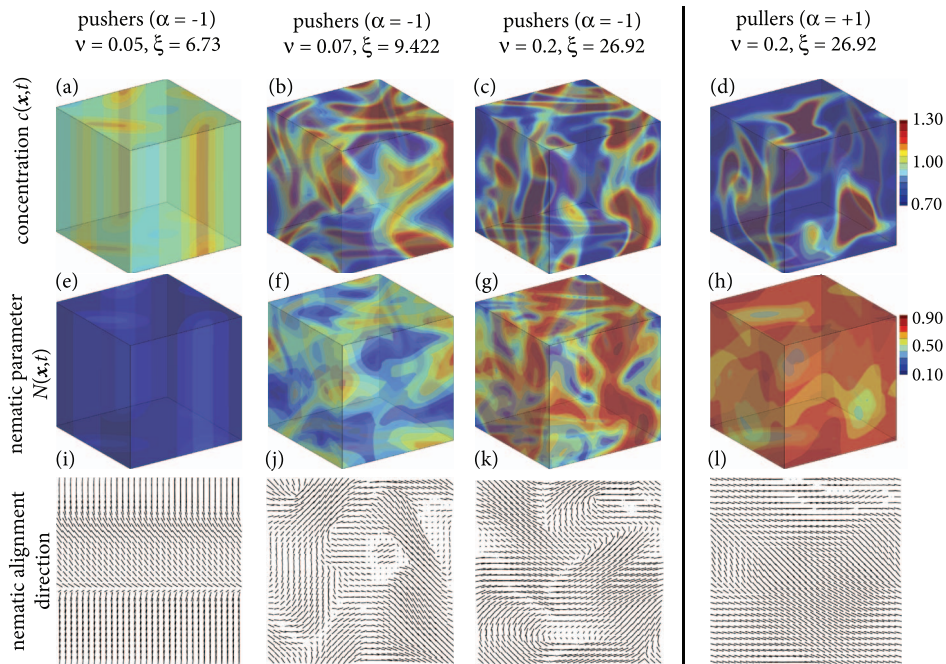


FIG. 9. Simulation results for pushers and pullers. Panels (a)–(d) show the concentration fields $c(\mathbf{x}, t)$ at an arbitrary time after the initial transient for the following cases: (a) pushers at $\nu = 0.05$, (b) pushers at $\nu = 0.07$, (c) pushers at $\nu = 0.2$, and (d) pullers at $\nu = 0.2$. Panels (e)–(h) show the corresponding nematic parameter fields $N(\mathbf{x}, t)$ defined in Eq. (70), for the same cases. Panels (i)–(l) show the nematic orientation fields in a two-dimensional slice, obtained by taking the eigenvector of $\mathbf{Q}(\mathbf{x}, t)$ with largest eigenvalue (enhanced online). [URL: <http://dx.doi.org/10.1063/1.4812822.1>]

B. Results and discussion

Figure 9 and accompanying video illustrate the dynamics in a number of simulations of pushers and pullers. Typical concentration fields observed in suspensions of pushers ($\alpha = -1$) are shown in Figs. 9(a)–9(c) for the volume fractions $\nu = 0.05, 0.07$, and 0.2 . In the first two cases, only the isotropic base state exists, as $\xi < \xi_1^c$. Based on the linear analysis of Sec. III C, the isotropic base state should be stable, in the long-wave limit, for $\xi < \xi^c \approx 0.039$ [obtained from Eq. (68)] and always unstable above this value. We indeed find that pusher suspensions are unstable for all three values of ν shown in Fig. 9, but stable when $\nu = 0.02$ (not shown). At the lowest unstable value of $\nu = 0.05$ [Fig. 9(a)], we find, however, that the instability is very weak and takes the form of two-dimensional concentration patterns; in the plane of the patterns, unsteady dynamics arise that are qualitatively very similar to our previous two-dimensional simulations of dilute suspensions.^{21,22} Further decreasing ν eventually stabilizes the system completely. The emergence of two-dimensional patterns close to the marginal stability condition is unexpected and not predicted by the linear analysis; it is reminiscent, however, of previous observations made on the dynamics of active pusher suspensions in shear flows,²⁷ where stabilization by the flow was also shown to lead to a transition from three- to two-dimensional instabilities. At the higher volume fraction of $\nu = 0.07$, which is still below the isotropic-to-nematic transition, three-dimensional unsteady concentration patterns arise, which are qualitatively similar to those previously observed in dilute instabilities.²⁷ These patterns continually form and break up in time, leading to chaotic dynamics. At the higher concentration of $\nu = 0.2$, which is above the isotropic-to-nematic transition, the patterns still persist and do not look significantly different; other statistics, however, such as the degree of particle alignment, will exhibit distinct features.

In the case of pullers ($\alpha = +1$), the linear stability results are also confirmed. We do find that the isotropic base state is always stable when $\xi < \xi_2^c$, and that the nematic branch is also stable for $\xi \gtrsim \xi_1^c$, see Fig. 8(c). At high values of ν or ξ , an instability is observed as shown in Fig. 9(d) for $\nu = 0.2$, and also takes the form of three-dimensional unsteady patterns. These patterns, however,

have a different morphology from those obtained in the case of pushers, and tend to have globular shapes compared to the sheets that pushers tend to form. The existence of this instability is truly a consequence of the combination of steric interactions and activity, as dilute suspensions of pullers were found to be always stable in previous work,^{22,27} and as concentrated suspensions of movers, for which $\alpha = 0$, are also observed to be stable in our simulations.

We characterize the local degree of nematic alignment of the particles by defining the following nematic parameter $N(\mathbf{x}, t)$:

$$N(\mathbf{x}, t) = \frac{3}{2} \left[-\min_{\mathbf{p} \in \Omega} \left(\frac{U(\mathbf{x}, \mathbf{p}, t)}{U_{0c}(\mathbf{x}, t)} \right) - \frac{1}{3} \right] = \frac{3}{2} \max_{\mathbf{p} \in \Omega} [\mathbf{p}\mathbf{p} : \mathbf{Q}(\mathbf{x}, t)] = \frac{3}{2} e_Q, \quad (70)$$

where e_Q is the largest eigenvalue of the nematic order parameter tensor $\mathbf{Q}(\mathbf{x}, t)$. It is straightforward to see that $N(\mathbf{x}, t) = 0$ for an isotropic orientation distribution, and 1 for a perfectly aligned distribution. Also note that for the base-state distributions we have $N = A[\Psi_0] = 4\delta/\xi$, with N tending to 1 as $\xi \rightarrow \infty$. The nematic parameter is illustrated in Figs. 9(e)–9(h), for the same cases as for the concentration field. In the case of pushers, the value of N is very low near the marginal stability limit ($\nu = 0.05$), which is a consequence of the dominant effect of rotational diffusion and explains the weak instability observed in this case. As ν increases, fluctuations in N become stronger, as does the overall level of alignment. This is especially clear when $\nu = 0.2$, where many large domains of very strong nematic alignment are present in the suspensions [Fig. 9(g)]. In the case of unstable puller suspensions [Fig. 9(h)], alignment is yet stronger, with N reaching values above 0.6 almost everywhere in the flow. A careful observation of the initial transient in the case of pullers, for instance in the video accompanying Fig. 9, reveals that the suspension, which is nearly isotropic in the initial condition, first quickly evolves towards the nematic base state, which then itself becomes destabilized; this interesting fact, which is not observed in the case of pushers, will be further discussed below.

Figures 9(i)–9(l) also show the nematic alignment field, obtained by calculating the eigenvector $\mathbf{s}(\mathbf{x}, t)$ of the tensor $\mathbf{Q}(\mathbf{x}, t)$ with eigenvalue e_Q . In pusher suspensions, orientations are spatially correlated over large length scales, although the strong fluctuations in the unstable regimes lead to finite domains of correlation separated by what appears to be defects. In unstable puller suspensions, we find that these defects become fewer, and the orientations are strongly correlated over the entire scale of the system.

The qualitative differences between unstable pusher and puller suspensions at high values of ξ can be interpreted based on the linear stability results. In the case of pushers, all steady base states are unstable when $\xi > \xi^c \approx 0.039$. We do not expect any significant qualitative changes in the dynamics when ν or ξ is further increased, as the nematic base state is never approached; the only clear feature occurring at very high concentrations is an enhancement of the local degree of alignment, as illustrated in Fig. 9(g). The case of pullers, however, is different: the isotropic state is stable up to the nematic transition, and a stable nematic state can also be observed close to the transition [Fig. 8(c)]; when increasing ξ further, this aligned configuration is also destabilized by activity (in agreement with previous analyses of aligned suspensions^{12,17,21,22}), leading to fluctuations close to the nematic equilibrium. This is precisely what is observed in Figs. 9(d) and 9(h), where the isotropic initial condition first becomes unstable, briefly giving way to a nematically aligned state, which subsequently also destabilizes and leads to fluctuations with a strong degree of alignment and long-ranged spatial orientation correlations. The dynamics described here are seen most clearly in Fig. 10, which shows the spatial average of the nematic parameter N as a function of time. Note that the initial non-zero value of $\langle N(t) \rangle$ in this figure is due to the initial perturbation introduced in the distribution function at $t = 0$, which is weakly anisotropic. In the case of pushers, we clearly see that unsteady dynamics emerge directly from the initial isotropic configuration, and that increasing ν really only modifies the mean degree of alignment at steady-state, with a stronger alignment occurring at the highest concentrations. In the case of pullers, we observe that the whole suspension first aligns nematically, with the mean degree of alignment quickly reaching a plateau at $N \approx 0.85$, which is very close to the theoretical value of $4\delta/\xi \approx 0.86$ for the nematic base state of branch 2

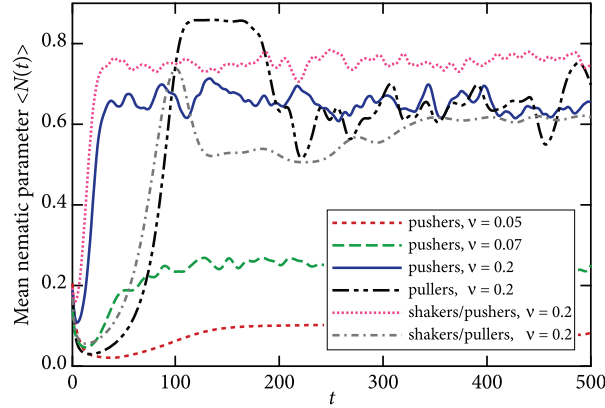


FIG. 10. Spatially averaged nematic parameter $\langle N(\mathbf{x}, t) \rangle$, defined in Eq. (70), as a function of time in suspensions of pushers ($\alpha = -1$), pullers ($\alpha = +1$), as well as shakers ($V_0 = 0$, $\alpha = \pm 1$) at various volume fractions.

when $\xi = 26.92$. After a short period, this nematic state subsequently destabilizes and the value N decreases again to fluctuate around a mean of 0.6.

All the instabilities described in Sec. III lead to the growth of the local nematic alignment of the particles, irrespective of their polar orientation. Indeed, all terms involving active stresses and steric effects in the kinetic model only involve the nematic order parameter tensor $\mathbf{Q}(\mathbf{x}, t)$ (as well as the fourth moment $\mathbf{S}(\mathbf{x}, t)$ through the steric and flow-induced stresses). However, our previous study of dilute suspensions²² has shown that the polar order parameter $\mathbf{n}(\mathbf{x}, t)$ also grows as a result of the instability, because an initially weak polarity exists in the initial condition. As argued in our previous work, this non-zero director field is precisely what leads to the growth of concentration fluctuations in the nonlinear regime, via the nonlinear source term appearing in the governing equation for the concentration field:

$$\partial_t c + \mathbf{u} \cdot \nabla_x c - D \nabla_x^2 c = -V_0 \nabla_x \cdot (c \mathbf{n}). \quad (71)$$

The same effect is observed in the present work, and results on the polar order parameter and its relation to the hydrodynamic velocity are illustrated in Fig. 11. The spatially averaged norm $\langle |\mathbf{n}(\mathbf{x}, t)| \rangle$ of the polar order parameter is shown as a function of time in Fig. 11(a) for the same simulations as in Fig. 9. In pusher suspensions, a clear net polarity is observed, which is weak close to the marginal stability limit ($\nu = 0.05$), but becomes quite strong at higher values of ν . Polarity also emerges in unstable puller suspensions, though it only grows once the nematic state is destabilized, and the steady-state value of $\langle |\mathbf{n}| \rangle$ is found to be significantly less than in pusher suspensions at the same volume fraction, even though both suspensions have nearly the same average value of the nematic parameter as seen in Fig. 10. Figure 11(b) also shows the magnitude of the hydrodynamic velocity averaged over space as a function of time. The fluid velocity shows similar trends as the polar order parameter: it increases with ν for pushers, and is typically weaker in unstable puller suspensions than in pusher suspensions at the same value of ξ . What is perhaps most unexpected is the different nature of the interaction between \mathbf{u} and \mathbf{n} in pusher and puller suspensions, as illustrated in Fig. 11(c) showing the spatial average of $\langle |\mathbf{n} + \mathbf{u}| \rangle$, which can be interpreted as an effective swimming velocity in the presence of hydrodynamic interactions. In the case of pushers, the effects of polar alignment and hydrodynamic flow are compounded, resulting in a net velocity that is of the order of $\langle |\mathbf{n}| \rangle + \langle |\mathbf{u}| \rangle$. Such is not the case for pullers, where the mean swimming motions due to the polarity impedes transport by the hydrodynamic flow.

These observations are easily explained by considering correlations between hydrodynamic velocity $\mathbf{u}(\mathbf{x}, t)$, polar order parameter $\mathbf{n}(\mathbf{x}, t)$, and nematic direction of alignment $\mathbf{s}(\mathbf{x}, t)$. Precisely, we define the following quantities:

$$C_1(t) = \frac{1}{V} \int_V c(\mathbf{x}, t) N(\mathbf{x}, t) \frac{|\mathbf{u}(\mathbf{x}, t) \cdot \mathbf{s}(\mathbf{x}, t)|}{|\mathbf{u}(\mathbf{x}, t)|} d\mathbf{x}, \quad (72)$$

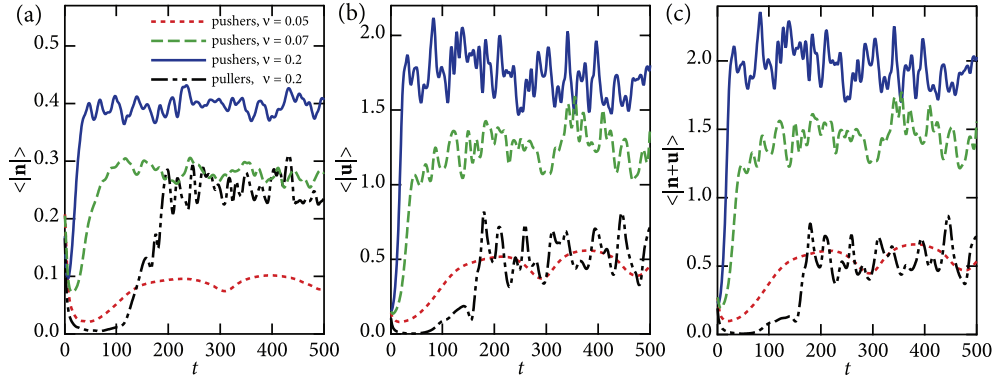


FIG. 11. Time evolution of the spatial averages of (a) $|\mathbf{n}(\mathbf{x}, t)|$, (b) $|\mathbf{u}(\mathbf{x}, t)|$, and (c) $|\mathbf{n}(\mathbf{x}, t) + \mathbf{u}(\mathbf{x}, t)|$, in suspensions of pushers at $v = 0.05, 0.07$, and 0.2 , and pullers at $v = 0.2$.

$$C_2(t) = \frac{1}{V} \int_V c(\mathbf{x}, t) N(\mathbf{x}, t) \frac{|\mathbf{n}(\mathbf{x}, t) \cdot \mathbf{s}(\mathbf{x}, t)|}{|\mathbf{u}(\mathbf{x}, t)|} d\mathbf{x}, \quad (73)$$

$$C_3(t) = \frac{1}{V} \int_V c(\mathbf{x}, t) \frac{\mathbf{u}(\mathbf{x}, t) \cdot \mathbf{n}(\mathbf{x}, t)}{|\mathbf{u}(\mathbf{x}, t)|} d\mathbf{x}, \quad (74)$$

which are plotted in Fig. 12 as functions of time. The function $C_1(t)$, which shows the correlation between the orientations of the hydrodynamic velocity and the nematic alignment direction $\mathbf{s}(\mathbf{x}, t)$ is plotted in Fig. 12(a): a net correlation is observed in all simulations, regardless of swimmer type, and becomes stronger at higher concentrations. This is not surprising, as the effect of the flow on orientation is precisely to align particles with the flow via Jeffery's equation in Eq. (5). More precisely, Jeffery's equation causes nematic alignment along the principal axis of maximum extension of the velocity gradient. As shown in Fig. 12(b), the nematic alignment direction is also strongly correlated with the direction of the polar order parameter $\mathbf{n}(\mathbf{x}, t)$, which again could have been expected. The difference between pushers and pullers is most clear in Fig. 12(c), which shows the function $C_3(t)$ characterizing the correlation between polar order parameter and hydrodynamic velocity. In the case of pushers, a positive correlation is found, corresponding to particles swimming preferentially in the same direction as the flow velocity; this is in agreement with the results of Fig. 11(c), where we found that the effects of \mathbf{u} and \mathbf{n} on the mean total swimmer velocity are compounded for pushers. The situation is quite different for pullers, where $C_3(t)$ is typically negative, indicating that pullers swim preferentially against the flow, resulting in an effective decrease in their total velocity as observed

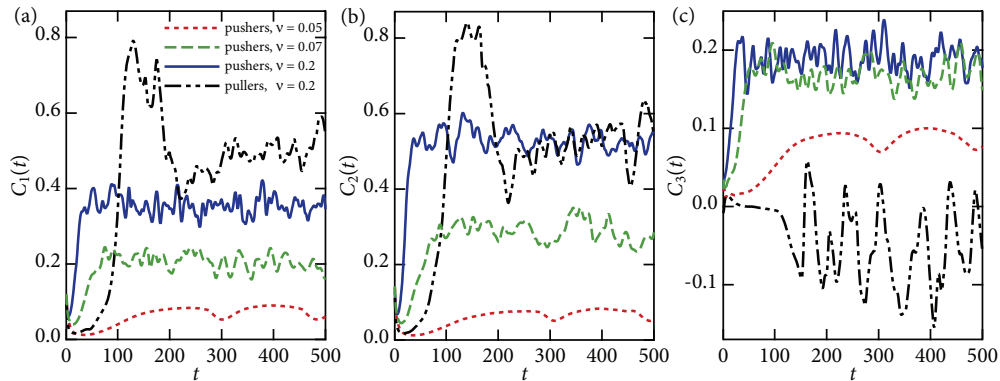


FIG. 12. Time evolution of the correlation defined in Eqs. (72)–(74): (a) $C_1(t)$, (b) $C_2(t)$, and (c) $C_3(t)$, in suspensions of pushers at $v = 0.05, 0.07$, and 0.2 , and pullers at $v = 0.2$.

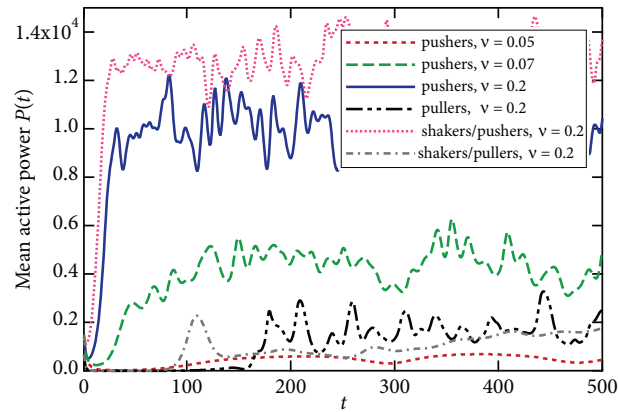


FIG. 13. Mean active power $P(t)$ defined in Eq. (75) as a function of time, in suspensions of pushers at $v = 0.05, 0.07,$ and $0.2,$ and pullers at $v = 0.2.$ The plot also shows results for shakers ($V_0 = 0, \alpha = \pm 1$) at $v = 0.2.$

in Fig. 11(c). While we do not yet have a complete explanation for this behavior, it is consistent with our previous particle simulations in the dilute and semi-dilute regimes, where we found that hydrodynamic interactions tend to enhance the mean swimming speed of pushers, but decrease that of pullers.^{17,18}

The hydrodynamic flows arising in the simulations are driven by the active stress exerted by the particles, which effectively injects mechanical energy into the system. The amount of active power transferred by the swimmers to the mean-field flow can be estimated by a simple mechanical energy balance on the momentum equation as follows:²²

$$P(t) = -\alpha \int_V \int_{\Omega} [\mathbf{pp} : \mathbf{E}(\mathbf{x}, t)] \Psi(\mathbf{x}, \mathbf{p}, t) d\mathbf{p} d\mathbf{x} = -\alpha \int_V \mathbf{E}(\mathbf{x}, t) : \mathbf{D}(\mathbf{x}, t) d\mathbf{x}, \quad (75)$$

where we see that power is directly linked to the relation between the nematic order parameter in the suspension and the local rate-of-strain tensor. In dilute systems,²² it was found that $P(t)$ increases in suspensions of pushers as a result of instabilities, but decreases to zero in suspensions of pullers,

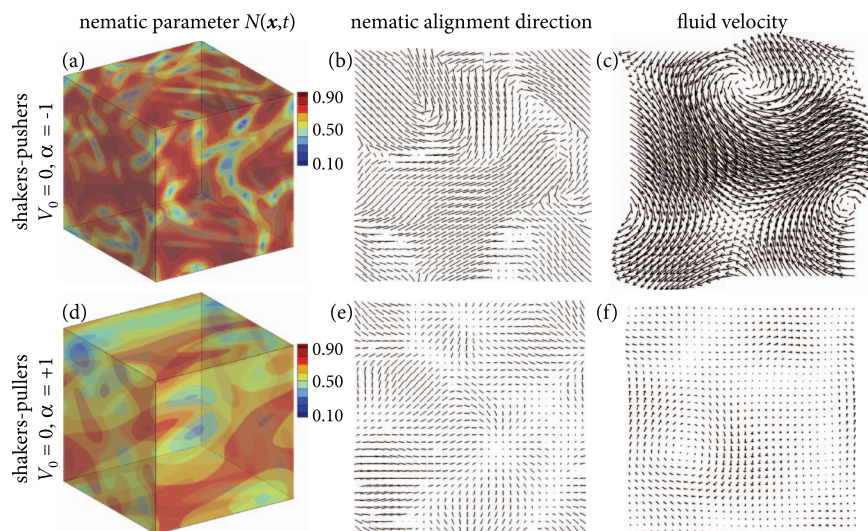


FIG. 14. Simulation results for shakers ($V_0 = 0$) at an effective volume fraction of $v = 0.2$ ($\xi = 26.92$). Panels (a)–(c) are for pushers ($\alpha = -1$) and (d)–(f) for pullers ($\alpha = +1$). (a) and (d) show the nematic parameter $N(\mathbf{x}, t)$ defined in Eq. (70); (b) and (e) show the nematic orientation fields in a two-dimensional slice, obtained by taking the eigenvector of $\mathbf{Q}(\mathbf{x}, t)$ with largest eigenvalue; and (c) and (f) show the hydrodynamic velocity fields in a two-dimensional slice.

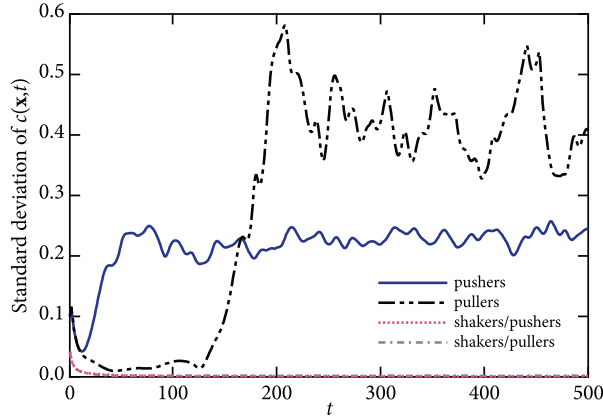


FIG. 15. Standard deviation $\sqrt{\langle(c-1)^2\rangle}$ of the concentration field $c(\mathbf{x}, t)$ as a function of time, in suspensions of pushers ($\alpha = -1$), pullers ($\alpha = +1$), and shakers ($V_0 = 0$) of both types, at $\nu = 0.2$.

which were always stable. Results for the present simulations are shown in Fig. 13. In agreement with the dilute case, pusher suspensions have a net positive power, which increases with increasing ν as the instabilities become stronger. In the case of unstable puller suspensions, a net positive power is also observed, though its value is significantly less than for pushers at the same concentration. Considering that the prefactor $-\alpha$ in Eq. (75) is of negative sign for pullers, this again hints at a fundamentally different type of interaction between particle orientations and local self-induced flow in puller suspensions, through the net negative sign of the product $\mathbf{E}(\mathbf{x}, t) : \mathbf{D}(\mathbf{x}, t)$.

We finish the discussion of our simulations by presenting results on suspensions of shakers, which are particles that drive active stresses (with α of either sign) but do not swim: $V_0 = 0$. The linear stability of shaker suspensions is the same as that of pusher or puller suspensions in the long-wave limit, as we saw in Sec. III that letting $k \rightarrow 0$ is equivalent to eliminating the convective term due to swimming in the linearized eigenvalue problem. We verify indeed in our simulations that instabilities arise in shaker suspensions (either pushers or pullers) according the same diagrams as obtained in Fig. 8, and lead to the local alignment of the particles and to the emergence of complex flows. Typical results for both types of shakers are shown in Fig. 14. We find that results for the nematic parameter, nematic alignment field, and hydrodynamic velocity field are very similar to what was obtained previously in the case of actual pushers and pullers. This is confirmed in Figs. 10 and 13, where shakers are seen to align as strongly and exert as much power as their swimming counterparts, if not more. One significant difference, however, is that shaker suspensions of either type are never subject to concentration instabilities, even in the nonlinear regime: the instability when $V_0 = 0$ only pertains to the particle orientations, and there is no mechanism for growth of concentration fluctuations. This is again easily understood by consideration of Eq. (71) for the concentration field, where the nonlinear source term $-V_0 \nabla_x \cdot (c\mathbf{n})$ vanishes when $V_0 = 0$. The evolution of the variance of the concentration field for pushers, pullers, and both types of shakers at the same concentration of $\nu = 0.2$ is illustrated in Fig. 15 and confirms this result. It is found that the variance quickly decays to zero in suspensions of shakers, even though strong fluctuations of the nematic parameter and velocity field are taking place. In suspensions of regular pushers and pullers, the concentration variance increases as expected and in agreement with the dynamics shown in Fig. 9.

V. CONCLUDING REMARKS

We have presented a continuum model for the dynamics in concentrated suspensions of hydrodynamically interacting active particles, such as swimming microorganisms or artificial microswimmers. The model is an extension of our previous theory for dilute suspensions,²² and is based on a Smoluchowski equation for the distribution of particle positions and orientations, coupled to the

Stokes equations for the fluid flow with an added stress arising from activity. In dense systems, this model is modified by addition of a steric interaction torque in the equation for the angular flux velocity, which causes neighboring particles to align. In addition, flow-induced stresses due to the inextensibility of the particles in the flow, and steric stresses resulting from direct contact interactions also have to be included in the concentrated regime. Based on this model, two types of uniform base-state solutions are possible: the isotropic state (branch 1), which exists for all concentrations; two nematic states (branches 2 and 3), which arise only above a critical value of $\xi = 2U_0v/d$. The nematic base state with the strongest alignment (branch 2) always realizes the minimum steric interaction energy for the system.

We first performed a linear stability analysis of these base states for pushers ($\alpha < 0$), movers ($\alpha = 0$), and pullers ($\alpha > 0$), as summarized in Fig. 8. Movers, which are particles that do not exert an active stress but still swim, are stable in the isotropic state up to $\xi = \xi_2^c = 15$; the nematic branch 2, which is subject to a weak instability as a result of the steric stress, is likely to be stable in a number of situations in finite systems (as it was found to be in our simulations). In the case of pushers, activity has a destabilizing effect: the isotropic state becomes unstable at a low value of ξ , and the nematic branches are always unstable. Pullers, however, are more stable than pushers: the isotropic state has the same stability as movers, and the nematic branch 2 is first stable over a finite range of values of ξ , but then becomes unstable at high ξ .

Numerical simulations of the kinetic equations confirmed all the results of the stability analysis. In particular, unstable chaotic solutions were obtained in suspensions of pushers even before the isotropic-to-nematic transition, whereas higher values of v were required to observe an instability in the case of pullers. While both types of swimmers are subject to instabilities at high concentrations, the characteristics of the flows that emerge in the nonlinear regime differ qualitatively. While the instability for pushers is only intensified by steric interactions which cause stronger particle alignment, the dynamics in the unstable regime are relatively unaffected as v increases above the nematic transition; on the other hand, the instability in puller suspensions appears to occur from the nematic state, and leads to fluctuations with very strong alignment but weaker hydrodynamic fluctuations and active power than for pushers.

These results again highlight the fundamentally different nature of interactions between particles and self-generated flows in suspensions of pushers and pullers, which has been reported previously in many contexts. Jeffery's equation, which governs the orientational dynamics of the swimmers in the fluid flow, causes all types of particles to align with the principal axes of the rate-of-strain tensor; however, pushers tend to drive extensional flows whereas pullers drive compressional flows. This important difference is clear for instance when considering the product $\mathbf{E}(\mathbf{x}, t) : \mathbf{D}(\mathbf{x}, t)$ appearing in the definition of the active power in Eq. (75): in the case of pushers, $\mathbf{E} : \mathbf{D}$ tends to be positive, whereas it tends to be negative in unstable puller suspensions.

A few limitations of the present model should be kept in mind. First, the expressions derived in Sec. II D are based on a dilute approximation, as they only consider the interaction of a single particle with a mean-field flow (in the case of the flow-induced stress) or with a mean-field orientation distribution (in the case of the steric stress). These expressions involve linear and quadratic corrections to the Newtonian stress in terms of volume fraction, but are unlikely to be quantitatively accurate in very dense systems, where more complex rheological laws would be needed. However, we do not expect the effects of these stresses to change qualitatively at high volume fractions. A perhaps greater limitation of the model is the one-fluid assumption in which particles have no volume, which allowed us to describe fluid and particle motions in terms of the same hydrodynamic velocity field. Nevertheless, we believe that the present model captures most salient features of interactions in concentrated active suspensions, and casts new light on the subtle interaction of hydrodynamic and steric effects in these systems.

ACKNOWLEDGMENTS

The authors thank E. Lushi for illuminating conversations on sterically induced stresses, and acknowledge funding from National Science Foundation (NSF) Grant Nos. DMS-0930930 and

DMS-0930931 and from the (U.S.) Department of Energy (DOE) Grant No. DE-FG02-88ER25053. Computational resources were provided by Teragrid Grant No. TG-CTS100007.

APPENDIX: STERIC STRESS TENSOR CALCULATION

In this appendix, we derive an expression for the stress tensor resulting from steric interactions, in the case of a suspension of slender rodlike particles. As discussed in Sec. II B, steric interactions result in an effective angular velocity given by Eq. (20):

$$\dot{\mathbf{p}} = 2U_0(\mathbf{I} - \mathbf{p}\mathbf{p}) \cdot \mathbf{D} \cdot \mathbf{p}, \quad (\text{A1})$$

where the second-order tensor \mathbf{D} is defined in Eq. (9). We model the particle dynamics using leading-order slender-body theory,⁶⁶ which for a stationary particle in a quiescent liquid simplifies to

$$s\dot{\mathbf{p}} = \frac{\ln(2r)}{4\pi\eta}(\mathbf{I} + \mathbf{p}\mathbf{p}) \cdot \mathbf{f}(s), \quad (\text{A2})$$

where $s \in [-\ell/2, \ell/2]$ is a linear coordinate along the axis of the particle, and $\mathbf{f}(s)$ denotes the linear force distribution along the rod. This expression can be inverted for the force distribution:

$$\mathbf{f}(s) = \frac{4\pi\eta}{\ln(2r)} \left(\mathbf{I} - \frac{1}{2}\mathbf{p}\mathbf{p} \right) \cdot s\dot{\mathbf{p}} = \frac{8\pi\eta U_0 s}{\ln(2r)} (\mathbf{I} - \mathbf{p}\mathbf{p}) \cdot \mathbf{D} \cdot \mathbf{p}. \quad (\text{A3})$$

Following Batchelor,⁵¹ the effective stress tensor in the suspension is then expressed as a configurational average of the stresslets, or first force moments, on the particles:

$$\Sigma^t(\mathbf{x}, t) = - \left\langle \int_{-\ell/2}^{\ell/2} \mathbf{f}(s) \mathbf{p} s ds \right\rangle = - \frac{\pi\eta\ell^3 U_0}{3 \ln(2r)} \langle (\mathbf{I} - \mathbf{p}\mathbf{p}) \cdot \mathbf{D} \cdot \mathbf{p}\mathbf{p} \rangle, \quad (\text{A4})$$

where $\langle \cdot \rangle$ denotes an orientational average:

$$\langle h \rangle = \int_{\Omega} h(\mathbf{p}) \Psi(\mathbf{x}, \mathbf{p}, t) d\mathbf{p}. \quad (\text{A5})$$

In index notation, Eq. (A4) becomes

$$\Sigma_{ij}^t = - \frac{\pi\eta\ell^3 U_0}{3 \ln(2r)} \langle (\delta_{ik} - p_i p_k) D_{kl} p_l p_j \rangle = - \frac{\pi\eta\ell^3 U_0}{3 \ln(2r)} [D_{il} \langle p_l p_j \rangle - \langle p_i p_j p_k p_l \rangle D_{kl}]. \quad (\text{A6})$$

Recalling that $\langle p_l p_j \rangle = D_{lj} + (c/3)\delta_{lj}$, where c is the concentration, we obtain

$$\Sigma_{ij}^t = - \frac{\pi\eta\ell^3 U_0}{3 \ln(2r)} \left[D_{il} (D_{lj} + \frac{c}{3}\delta_{lj}) - \langle p_i p_j p_k p_l \rangle D_{kl} \right]. \quad (\text{A7})$$

After subtracting an isotropic tensor, which does not affect the velocity of the flow and only modifies the pressure, we arrive at the final expression:

$$\Sigma^t(\mathbf{x}, t) = -\sigma_t \left[\mathbf{D}(\mathbf{x}, t) \cdot \mathbf{D}(\mathbf{x}, t) + \frac{c(\mathbf{x}, t)}{3} \mathbf{D}(\mathbf{x}, t) - \mathbf{S}(\mathbf{x}, t) : \mathbf{D}(\mathbf{x}, t) \right], \quad (\text{A8})$$

where $\sigma_t = \pi\eta\ell^3 U_0 / 3 \ln(2r)$ and the fourth-order tensor \mathbf{S} is defined in Eq. (10).

¹N. H. Mendelson, A. Bourque, K. Wilkening, K. R. Anderson, and J. C. Watkins, "Organized cell swimming motions in *Bacillus subtilis* colonies: Patterns of short-lived whirls and jets," *J. Bacteriol.* **181**, 600 (1999).

²C. Dombrowski, L. Cisneros, S. Chatkaew, R. E. Goldstein, and J. O. Kessler, "Self-concentration and large-scale coherence in bacterial dynamics," *Phys. Rev. Lett.* **93**, 098103 (2004).

³A. Sokolov, R. E. Goldstein, F. I. Feldchtein, and I. S. Aranson, "Enhanced mixing and spatial instability in concentrated bacterial suspensions," *Phys. Rev. E* **80**, 031903 (2009).

⁴H. Kurtuldu, J. S. Guasto, K. A. Johnson, and J. P. Gollub, "Enhancement of biomixing by swimming algal cells in two-dimensional films," *Proc. Natl. Acad. Sci. U.S.A.* **108**, 10391 (2011).

⁵A. Sokolov, I. S. Aranson, J. O. Kessler, and R. E. Goldstein, "Concentration dependence of the collective dynamics of swimming bacteria," *Phys. Rev. Lett.* **98**, 158102 (2007).

⁶L. H. Cisneros, R. Cortez, C. Dombrowski, R. E. Goldstein, and J. O. Kessler, "Fluid dynamics of self-propelled microorganisms: From individuals to concentrated populations," *Exp. Fluids* **43**, 737 (2007).

- ⁷L. H. Cisneros, J. O. Kessler, S. Ganguly, and R. E. Goldstein, "Dynamics of swimming bacteria: Transition to directional order at high concentration," *Phys. Rev. E* **83**, 061907 (2011).
- ⁸T. Ishikawa, "Suspension biomechanics of swimming microbes," *J. R. Soc., Interface* **6**, 815 (2009).
- ⁹S. Ramaswamy, "The mechanics and statistics of active matter," *Annu. Rev. Condens. Matter Phys.* **1**, 323 (2010).
- ¹⁰D. L. Koch and G. Subramanian, "Collective hydrodynamics of swimming microorganisms: Living fluids," *Annu. Rev. Fluid Mech.* **43**, 637 (2011).
- ¹¹D. Saintillan and M. J. Shelley, "Active suspensions and their nonlinear models," *C. R. Phys.* (in press).
- ¹²R. Aditi Simha and S. Ramaswamy, "Hydrodynamic fluctuations and instabilities in ordered suspensions of self-propelled particles," *Phys. Rev. Lett.* **89**, 058101 (2002).
- ¹³I. S. Aranson, A. Sokolov, J. O. Kessler, and R. E. Goldstein, "Model for dynamical coherence in thin films of self-propelled microorganisms," *Phys. Rev. E* **75**, 040901 (2007).
- ¹⁴C. W. Wolgemuth, "Collective swimming and the dynamics of bacterial turbulence," *Biophys. J.* **95**, 1564 (2008).
- ¹⁵J. P. Hernández-Ortiz, C. G. Stoltz, and M. D. Graham, "Transport and collective dynamics in suspensions of confined self-propelled particles," *Phys. Rev. Lett.* **95**, 204501 (2005).
- ¹⁶P. T. Underhill, J. P. Hernández-Ortiz, and M. D. Graham, "Diffusion and spatial correlations in suspensions of swimming particles," *Phys. Rev. Lett.* **100**, 248101 (2008).
- ¹⁷D. Saintillan and M. J. Shelley, "Orientational order and instabilities in suspensions of self-locomoting rods," *Phys. Rev. Lett.* **99**, 058102 (2007).
- ¹⁸D. Saintillan and M. J. Shelley, "Emergence of coherent structures and large-scale flows in motile suspensions," *J. R. Soc., Interface* **9**, 571 (2012).
- ¹⁹T. Ishikawa and T. J. Pedley, "Coherent structures in monolayers of swimming particles," *Phys. Rev. Lett.* **100**, 088103 (2008).
- ²⁰T. Ishikawa, J. T. Locsei, and T. J. Pedley, "Development of coherent structures in concentrated suspensions of swimming model micro-organisms," *J. Fluid Mech.* **615**, 401 (2008).
- ²¹D. Saintillan and M. J. Shelley, "Instabilities and pattern formation in active particle suspensions: Kinetic theory and continuum simulations," *Phys. Rev. Lett.* **100**, 178103 (2008).
- ²²D. Saintillan and M. J. Shelley, "Instabilities, pattern formation, and mixing in active suspensions," *Phys. Fluids* **20**, 123304 (2008).
- ²³G. Subramanian and D. L. Koch, "Critical bacterial concentration for the onset of collective swimming," *J. Fluid Mech.* **632**, 359 (2009).
- ²⁴M. Doi and S. F. Edwards, *The Theory of Polymer Dynamics* (Oxford University Press, Oxford, 1986).
- ²⁵Y. Hatwalne, S. Ramaswamy, M. Rao, and R. Aditi Simha, "Rheology of active-particle suspensions," *Phys. Rev. Lett.* **92**, 118101 (2004).
- ²⁶C. Hohenegger and M. J. Shelley, "Stability of active suspensions," *Phys. Rev. E* **81**, 046311 (2010).
- ²⁷A. Alizadeh Pahlavan and D. Saintillan, "Instability regimes in flowing suspensions of swimming micro-organisms," *Phys. Fluids* **23**, 011901 (2011).
- ²⁸N. C. Darnton, L. Turner, S. Rojevsky, and H. C. Berg, "Dynamics of bacterial swarming," *Biophys. J.* **98**, 2082 (2010).
- ²⁹H. P. Zhang, A. Be'er, E.-L. Florin, and H. L. Swinney, "Collective motions and density fluctuations in bacterial colonies," *Proc. Natl. Acad. Sci. U.S.A.* **107**, 13626 (2010).
- ³⁰X. Chen, X. Dong, A. Be'er, H. L. Swinney, and H. P. Zhang, "Scale-invariant correlations in dynamical bacterial clusters," *Phys. Rev. Lett.* **108**, 148101 (2012).
- ³¹N. Sambelashvili, A. W. C. Lau, and D. Cai, "Dynamics of bacterial flow: Emergence of spatiotemporal coherent structures," *Phys. Lett. A* **360**, 507 (2007).
- ³²A. Baskaran and M. C. Marchetti, "Statistical mechanics and hydrodynamics of bacterial suspensions," *Proc. Natl. Acad. Sci. U.S.A.* **106**, 15567 (2009).
- ³³M. G. Forest, Q. Wang, and R. Zhou, "Kinetic theory and simulations of active polar liquid crystalline polymers," *Soft Matter* **9**, 5207 (2013).
- ³⁴G. B. Jeffery, "The motion of ellipsoidal particles immersed in a viscous fluid," *Proc. R. Soc. London, Ser. A* **102**, 161 (1922).
- ³⁵F. P. Bretherton, "The motion of rigid particles in a shear flow at low Reynolds number," *J. Fluid Mech.* **14**, 284 (1962).
- ³⁶T. Ishikawa and M. Hota, "Interaction of two swimming *Paramecia*," *J. Exp. Biol.* **209**, 4452 (2006).
- ³⁷M. Doi and S. F. Edwards, "Dynamics of rod-like macromolecules in concentrated solution," *J. Chem. Soc., Faraday Trans. II* **74**, 560 (1978).
- ³⁸P. G. de Gennes and J. Prost, *The Physics of Liquid Crystals* (Clarendon Press, Oxford, 1993).
- ³⁹P. G. de Gennes, "Phenomenology of short-range-order effects in the isotropic phase of nematic materials," *Phys. Lett. A* **30**, 454 (1969).
- ⁴⁰A. N. Beris and B. J. Edwards, *Thermodynamics of Flowing Systems* (Oxford University Press, Oxford, 1994).
- ⁴¹T. B. Liverpool and M. C. Marchetti, "Hydrodynamics and rheology of active polar filaments," in *Cell Motility*, edited by P. Lenz (Springer, New York, 2008).
- ⁴²M. E. Cates, O. Heinrich, D. Marenduzzo, and K. Stratford, "Lattice-Boltzmann simulations of liquid crystalline fluids: Active gels and blue phases," *Soft Matter* **5**, 3791 (2009).
- ⁴³A. Baskaran and M. C. Marchetti, "Hydrodynamics of self-propelled hard rods," *Phys. Rev. E* **77**, 011920 (2008).
- ⁴⁴A. Baskaran and M. C. Marchetti, "Nonequilibrium statistical mechanics of self-propelled hard rods," *J. Stat. Mech.: Theor. Exp.* **2010**, P04019.
- ⁴⁵L. Onsager, "The effects of shapes on the interaction of colloidal particles," *Ann. N.Y. Acad. Sci.* **51**, 627 (1949).
- ⁴⁶W. Maier and A. Saupe, "Eine einfache molekulare Theorie des nematischen kristallinflüssigen Zustandes," *Z. Naturforsch.* **A 13A**, 564 (1958).

- ⁴⁷ K. Drescher, J. Dunkel, L. H. Cisneros, S. Ganguly, and R. E. Goldstein, "Fluid dynamics and noise in bacterial cell-cell and cell-surface scattering," *Proc. Natl. Acad. Sci. U.S.A.* **108**, 10940 (2011).
- ⁴⁸ M. Garcia, B. Stefano, P. Peyla, and S. Raaij, "Random walk of a swimmer in a low-Reynolds-number medium," *Phys. Rev. E* **83**, 035301 (2011).
- ⁴⁹ H. Brenner, "A general theory of Taylor dispersion phenomena," *PCH, PhysicoChem. Hydrodyn.* **1**, 91 (1980).
- ⁵⁰ P. D. Cobb and J. E. Butler, "Simulations of concentrated suspensions of rigid fibers: Relationship between short-time diffusivities and the long-time rotational diffusion," *J. Chem. Phys.* **123**, 054908 (2005).
- ⁵¹ G. K. Batchelor, "The stress system in a suspension of force-free particles," *J. Fluid Mech.* **41**, 545 (1970).
- ⁵² G. K. Batchelor, "Transport properties of two-phase materials with random structure," *Annu. Rev. Fluid Mech.* **6**, 227 (1974).
- ⁵³ D. Saintillan, "The dilute rheology of swimming suspensions: A simple kinetic model," *Exp. Mech.* **50**, 1275 (2010).
- ⁵⁴ K. Drescher, R. E. Goldstein, N. Michel, M. Polin, and I. Tuval, "Direct measurement of the flow field around swimming microorganisms," *Phys. Rev. Lett.* **105**, 168101 (2010).
- ⁵⁵ J. S. Guasto, K. A. Johnson, and J. P. Gollub, "Oscillatory flows induced by microorganisms swimming in two dimensions," *Phys. Rev. Lett.* **105**, 168102 (2010).
- ⁵⁶ D. Saintillan, "Kinetic models for biologically active suspensions," in *IMA Volume on Natural Locomotion in Fluids and on Surfaces: Swimming, Flying, and Sliding*, edited by S. Childress, A. Hosoi, W. W. Schultz, and Z. J. Wang (Springer, New York, 2012).
- ⁵⁷ E. J. Hinch and L. G. Leal, "Effect of Brownian motion on rheological properties of a suspension of non-spherical particles," *J. Fluid Mech.* **52**, 683 (1972).
- ⁵⁸ E. J. Hinch and L. G. Leal, "Constitutive equations in suspension mechanics. 2. Approximate forms for a suspension of rigid particles affected by Brownian rotations," *J. Fluid Mech.* **76**, 187 (1976).
- ⁵⁹ E. Lushi has also developed a numerical method for suspensions of interacting discrete swimmers that accounts for steric interactions and for this extra stress contribution, personal communication (2013).
- ⁶⁰ In rare situations, the active stress and the flow-induced stress can exhibit the same scaling with concentration: such is the case for instance at the marginal stability limit as was previously discussed by Subramanian and Koch.²³
- ⁶¹ E. S. G. Shaqfeh and G. H. Fredrickson, "The hydrodynamic stress in a suspension of rods," *Phys. Fluids A* **2**, 7 (1990).
- ⁶² D. J. Jeffrey, J. F. Morris, and J. F. Brady, "The pressure moments for two spheres in a low-Reynolds-number flow," *Phys. Fluids A* **5**, 2317 (1993).
- ⁶³ P. R. Nott and J. F. Brady, "Pressure-driven flow of suspensions: Simulation and theory," *J. Fluid Mech.* **275**, 157 (1994).
- ⁶⁴ P. R. Nott, E. Guazzelli, and O. Pouliquen, "The suspension balance model revisited," *Phys. Fluids* **23**, 043304 (2011).
- ⁶⁵ H. Hasimoto, "On the periodic fundamental solutions of the Stokes equations and their application to viscous flow past a cubic array of spheres," *J. Fluid Mech.* **5**, 317 (1959).
- ⁶⁶ G. K. Batchelor, "Slender-body theory for particles of arbitrary cross-section in Stokes flow," *J. Fluid Mech.* **44**, 419 (1970).